

Optimal Estimation Retrieval Framework for Daytime Clear-Sky Total Column Water Vapour from MTG-FCI Near-Infrared Measurements

Jan El Kassar^{1,3}, Cintia Carbajal Henken¹, Xavier Calbet², Pilar Rípodas², Rene Preusker¹, and Jürgen Fischer^{1,3}

¹Institute of Meteorology, Freie Universität Berlin, Carl-Heinrich-Becker-Weg 6-10, 12165 Berlin, Germany

²Agencia Estatal de Meteorología, Leonardo Prieto Castro 8, Ciudad Universitaria, 28071 Madrid, Spain

³Spectral Earth GmbH, Baseler Str. 91a, 12205 Berlin, Germany

Correspondence: Jan El Kassar, jan.elkassar@met.fu-berlin.de; Tel.: +49-30-838-64876

Abstract. A retrieval of total column water vapour (TCWV) from the new daytime, clear-sky near-infrared measurements of the Flexible Combined Imager (FCI) on-board the geostationary satellite Meteosat Third Generation Imager (MTG-I, Meteosat-12) is presented. The retrieval algorithm is based on the differential absorption technique, relating TCWV amounts to the radiance ratio of a non-absorbing band at 0.865 μm and a nearby WV absorbing band at 0.914 μm . The sensitivity of the band ratio to 5 WV amount increases towards the surface, which means the whole atmospheric column down to the boundary layer moisture variability can be observed well.

The retrieval framework is based on an Optimal Estimation (OE) method providing pixel-based uncertainty estimates. It builds on well-established algorithms successfully applied to other passive imagers with similar spectral band settings. Transferring knowledge gained in their development onto FCI required some new approaches. The absence of additional, adjacent 10 window bands to estimate the surface reflectance within FCI's absorbing channel are mitigated using a Principal Component Regression (PCR) from the bands at 0.51, 0.64, 0.865, 1.61, and 2.25 μm .

We utilize synergistic observations from OLCI and SLSTR to generate "FCI-like" measurements. OLCI bands were complemented with SLSTR observations, enabling evaluation of the retrieval's robustness and global performance of the PCR. Furthermore, this enables algorithm testing under realistic conditions using well-characterized data, at a time when a long-15 term, fully calibrated FCI Level 1c dataset was not yet available. We build a forward model for two FCI equivalent NIR bands (0.865 and 0.9 μm) on the Sentinel-3 Ocean and Land Colour Instrument (OLCI). A long-term validation of OLCI against a single Atmospheric Radiation Measurement (ARM) reference site without the PCR resulted in a bias of 1.85 kg/m^2 , cRMSE of 1.26 kg/m^2 and R^2 of 0.995.

A first verification of the OLCI/SLSTR "FCI-like" TCWV against well-established ground-based TCWV products concludes 20 with a wet bias between 0.33 – 2.84 kg/m^2 , a cRMSE between 1.46 – 2.21 kg/m^2 and R^2 between 0.98 – 0.99. In this set of comparisons, only land pixels were considered. Furthermore, a dataset of FCI Level 1c observations with a preliminary calibration was processed. The TCWV processed for these FCI measurements aligns well with reanalysis TCWV and collocated

OLCI/SLSTR TCWV but show a dry bias. A more rigorous validation and assessment will be done once a longer record of FCI data is available.

25 TCWV observations derived from geostationary satellite measurements enhance monitoring of WV distributions and associated meteorological phenomena from synoptic scales down to local scales. Such observations are of special interest for the advancement of nowcasting techniques and Numerical Weather Prediction (NWP) accuracy as well as process-studies.

1 Introduction

Water vapour (WV) is the fundamental ingredient in the formation of clouds and precipitation. Spatio-temporal WV distributions and fluxes impact the intensity and duration of precipitation. The presence of sufficient low-level moisture in the atmospheric boundary layer facilitates the formation of convective development through enhancement of atmospheric instability and also contributes to storm severity by acting as a source of energy, once a storm has initiated (e.g., Johns and Doswell, 1992; Doswell et al., 1996; Fabry, 2006; Púčik et al., 2015; Peters et al., 2017). On a global, climatological scale, WV is a major contributor to global energy fluxes and, due to its abundance and absorption over a wide range of the solar and terrestrial spectrum, acts as the strongest greenhouse gas (e.g. Trenberth et al., 2003; Schmidt et al., 2010). Within a changing climate, a warmer atmosphere will contain more WV which may form a positive feedback loop and further enhance global warming. Moreover, a moister atmosphere is predicted to produce more severe weather (e.g., Allen and Ingram, 2002; Neelin et al., 2022; Chen and Dai, 2023). Apart from that, WV is considered an inconvenient atmospheric component for several remote sensing applications for which precise information on WV amounts in the atmosphere are needed for atmospheric correction methods (e.g. Gao et al., 2009; Wiegner and Gasteiger, 2015; Valdés et al., 2021).

Observations of total column water vapour (TCWV) from satellite-based passive imagers operating in the visible (VIS), near-infrared (NIR) and thermal infrared (TIR) spectral range play a key role in monitoring its distribution at regional to global scales. WV retrievals using TIR measurements have a long heritage and are widely used, particularly from geostationary satellite platforms. On the one hand, a split-window technique using weakly absorbing WV measurements can be employed to retrieve TCWV or boundary layer WV with relatively high uncertainties (e.g., Kleespies and McMillin, 1990; Casadio et al., 2016; Hu et al., 2019; Dostalek et al., 2021; El Kassar et al., 2021). Lindsey et al. (2014) and Lindsey et al. (2018) showed that the split-window difference by itself may already provide valuable insight on the WV content in the boundary layer or lowest layers of the troposphere. On the other hand, measurements from strongly absorbing WV bands serve to retrieve WV amounts limited to upper tropospheric levels and/or layered WV products (e.g., Koenig and De Coning, 2009; Martinez et al., 2022). However, due to the absorption and re-emission of radiation by WV in the IR, such approaches rely on knowledge of the atmospheric temperature profile in addition to the atmospheric WV profile. Using observations in the VIS/NIR largely avoids these temperature-related complications.

The use of the so-called $\rho\sigma\tau$ WV absorption region in the NIR (0.9 to 1.0 μm) is not new. This designation stems from first observations of atmospheric absorption of solar radiation in the 19th century (Langley, 1902). There, light is more likely 55 to be absorbed by WV molecules compared to spectral regions outside these absorption features (window regions). These

NIR measurements exhibit the greatest sensitivity to WV amounts near the surface. Consequently, this allows for the retrieval of accurate clear-sky TCWV fields as well as providing information on changes of WV amounts in the lower troposphere. For several decades, the $\rho\sigma\tau$ region has been researched using radiative transfer models and exploited in TCWV retrieval schemes (e.g., Fischer, 1988; Gao and J., 1992; Bennartz and Fischer, 2001; Albert et al., 2005; Lindstrot et al., 2012; Diedrich et al., 2015; Preusker et al., 2021). The focus first lay on ground-based radiometers and soon shifted to airborne and space-borne imagers. The first satellites that carried instruments with dedicated NIR WV bands were almost exclusively on satellite platforms with sun-synchronous, polar orbits and could deliver global daily coverage at a km to hm resolution on a daily basis. Even at a km resolution, NIR TCWV can resolve convective phenomena such as horizontal convective rolls or gravity waves (Carabajal Henken et al., 2015; Lyapustin et al., 2014). Current NIR TCWV products, only available on polar orbits, provide accurate, highly-resolved TCWV but lack temporal resolution and may introduce observation biases in climatologies (Diedrich et al., 2016; Carabajal Henken et al., 2020).

The new Meteosat Third Generation Imager (MTG-I, hereinafter referred to as MTG) carries the Flexible Combined Imager (FCI) (Holmlund et al., 2021; Martin et al., 2021). The European Organisation for the Exploitation of Meteorological Satellites (EUMETSAT) commissions this third generation of European geostationary meteorological satellites for monitoring weather and climate. FCI is the successor to the Spinning Enhanced Visible and Infrared Imager (SEVIRI) (Schmetz et al., 2002) and will enhance the temporal and spatial resolution of geostationary remote sensing observations. Also, an expanded set of spectral channels compared to SEVIRI allows for more comprehensive observations of atmospheric and surface properties. FCI includes a new NIR WV absorption band not available on any other instrument onboard a geostationary platform to date. This band is located within the $\rho\sigma\tau$ WV absorption region at 0.914 μm .

The introduction of MTG and its new FCI NIR band will expand our ability to quantify and characterize local to global-scale WV distributions and monitor their changes. This has important implications for both weather and climate research and applications. Particularly in the domain of nowcasting, FCI's fine-scale observation of TCWV could substantially advance the field (e.g., Benevides et al., 2015; Van Baelen et al., 2011; Dostalek et al., 2021). The Satellite Application Facility on Support to Nowcasting and Very Short Range Forecasting (NWCSAF) is an organisation funded by EUMETSAT and aims to support meteorological services with satellite data critical for the prediction of high-impact weather (e.g., storms, fog). They commission, develop and maintain software which utilises many weather satellite instruments, including MTG-FCI/Meteosat-12 (García-Pereda et al., 2019). A NIR TCWV product in the portfolio of NWCSAF's software will greatly benefit the nowcasting and meteorological community at large.

In this work, we present our TCWV retrieval framework utilizing the novel NIR measurements obtained from MTG-FCI. Our approach builds on established TCWV retrieval frameworks successfully applied to other passive imagers sharing similar spectral band configurations. The differential absorption technique, using the ratio of measurements in the $\rho\sigma\tau$ -absorption band and nearby window bands, was previously employed in measurements of the Medium Resolution Imaging Spectrometer (MERIS) onboard Envisat (Bennartz and Fischer, 2001; Lindstrot et al., 2012). With the launch of the Copernicus Sentinel-3A and Sentinel-3B satellites (Donlon et al., 2012) and onboard Ocean and Land Colour Imager (OLCI), the retrieval framework has been extended to fully exploit OLCI's extended spectral capabilities by using multiple bands sensitive to WV absorption

(Preusker et al., 2021). Operational and calibrated FCI Level 1c data only became available at the end of 2024. Due to the unique technical characteristics of FCI as well as the limited availability of a well-calibrated FCI data record at the time this work was conducted, new strategies are imperative for our methodology and its assessment. One key element is the surface reflectance approximation method for the absorption band, which can be assessed with the use of OLCI-SLSTR "FCI-like" 95 data. In particular, we applied the same forward model and inversion principles to OLCI band 17 (0.865 μm) and band 19 (0.9 μm) as were used for FCI. The use of the OLCI/SLSTR synergy provides us with a formidable opportunity to establish an adapted retrieval framework and enables a robust testbed to explore algorithm performance accordingly. Additionally, OLCI Level 1b has well-known radiometric characterization and worldwide coverage, allowing for a practical and reliable basis to 100 assess and refine the retrieval framework under a wide range of realistic atmospheric and surface conditions.

100 The structure of this paper is as follows. Section 2 introduces the MTG-FCI data, OLCI-SLSTR data, auxiliary data, and the TCWV reference datasets, along with the associated matchup method. Section 3 details the MTG-FCI TCWV retrieval framework, covering the physical background, forward model, inversion method, albedo approximation method integral to the algorithm, and the finalized retrieval framework. Section 4 presents the results of the matchup assessments conducted on both 105 local and global scales, along with initial analyses using a preliminary calibrated MTG-FCI dataset and a representative case study. Section 5 provides a discussion and outlook, and Sect. 6 concludes the paper.

2 Data

2.1 MTG-FCI Data

MTG is an operational EUMETSAT satellite mission which currently consists of one satellite in geosynchronous orbit at 0° longitude. It carries the Lightning Imager (LI) and the FCI which is a multispectral instrument that scans with a fast east-west 110 and a slow north-south motion. It has 16 bands which range from the VIS (0.44 μm) to the TIR (13.3 μm). The full-disk scan service covers approximately one-fourth of the Earth's surface within 10 minutes, covering Europe, Africa, and parts of the Atlantic and Indian oceans (Durand et al., 2015; Holmlund et al., 2021). In the future, a second MTG-FCI will provide 115 a rapid scan service, which covers the northern third of the full-disk within 2.5 minutes, covering parts of Europe and the Mediterranean. The spatial resolution at sub-satellite point (SSP) of one VIS band at 0.64 μm and one SWIR band at 2.25 μm is 0.5 km. The spatial resolution of the other VIS to SWIR bands and the TIR bands at 3.8 μm and 10.5 μm is 1.0 km at SSP. The remaining TIR bands have an SSP resolution of 2.0 km. Due to the curvature of the Earth, the actual spatial resolution 120 outside the SSP is slightly lower. E.g., the 1 km SSP resolution (VIS, NIR and 10.5 μm) in Northern Europe is closer to 2.0 to 3.0 km.

MTG1 was launched successfully into orbit on 13th of December 2022, and currently the mission is still in the commissioning phase. Because of that, we use the latest release of preliminary MTG-FCI Level 1c data provided by EUMETSAT in 120 February 2024 (EUMETSAT, 2024b). They consist of one full-disk scene from 13th January 2024 between 11:50 and 12:00 UTC. They were downloaded from EUMETSAT's sftp server at <https://user.eumetsat.int/news-events/news/new-mtg-fci-test-dataset-mtgtd-505> and more details on this dataset can be found in EUMETSAT (2024a). At the time of publication, no

cloud mask is readily available for the FCI test data. Therefore, we built a simple cloud mask algorithm. The cloud masking
125 algorithm is largely based on the work presented in Hünerbein et al. (2023). In this publication, the authors adapted and
extended cloud masking and typing algorithms developed for NASA's Aqua/Terra Moderate Imaging Spectrometer (MODIS)
(Ackerman et al., 2002) to ESA's Cloud Aerosol and Radiation Explorer Mission (EarthCARE) Multi Spectral Imager (MSI).
We adapted a subset of their tests to the FCI bands and estimated new coefficients and thresholds. Eventually, the cloud mask
consists of two tests: threshold tests for reflectances, a reflectance ratio or the Global Environmental Monitoring Index (GEMI)
130 Pinty and Verstraete (1992).

2.2 S3-OLCI/SLSTR Data

Sentinel-3 is an operational COPERNICUS satellite mission of the European Commission, managed by EUMETSAT. It consists of two sister satellites (Sentinel-3A: S3A; Sentinel-3B: S3B) which orbit the Earth at an altitude of 814.5 km, an inclination of 98.65 ° and a local equator crossing time of 10:00 AM. S3B is phase-shifted to S3A by 140 °. This way, the
135 imaging instruments onboard the two satellites achieve global coverage almost daily. The payloads consist of the Synthetic Aperture Radar Altimeter (SRAL), supported by the Microwave Radiometer (MWR), the Sea and Land Surface Temperature Radiometer (SLSTR), and OLCI.

OLCI is a push-broom multispectral imaging spectrometer that consists of five cameras. It measures at 21 bands ranging from the VIS (0.4 μm) to the NIR (1.02 μm). The swath-width of OLCI is 1215 km at a full SSP resolution of 0.3 km per pixel,
140 which is referred to as "Full Resolution". In the "Reduced Resolution", 4 by 4 pixels are aggregated into 1.2 km pixels. This is the resolution used in this study. A characteristic of OLCI is an across-track spectral shift due to the five discrete cameras. This can be corrected for by taking into account the actual central wavelength at each of the across-track pixels (Preusker et al., in prep.).

SLSTR is a conical scanning multispectral, multi-angle radiometer. It measures at eight discrete bands ranging from the mid
145 VIS (0.55 μm) to the TIR (12.02 μm). The nadir-viewing swath width is 1400 km, and the oblique/rear-viewing swath width is 740 km. In the VIS to SWIR bands, SLSTR has a spatial resolution of 0.5 km at SSP, in the TIR (3 μm to 12.02 μm), the spatial resolution is 1 km at SSP. In the current two-satellite constellation, nadir-view global coverage is achieved within one day.

In order to mimic the capabilities of FCI at a similar spatial resolution and with similar spectral characteristics, we collocated
150 SLSTR observations to the OLCI grid using nearest-neighbour sampling. The used SLSTR bands are S5 (1.612 μm , 0.5 km) and S6 (2.25 μm , 0.5 km). They have been mapped to OLCI's reduced resolution at 1.2 km. Using Sentinel-3A and B, a representative set of swaths was created for every month of the year 2021 which amounts to a total of 1800 swaths across 80 days. The Identification of Pixel features (IdePIX) cloud detection algorithm was used to create cloud masks (Iannone et al., 2017; Wevers et al., 2021; Skakun et al., 2022).

2.3 ECMWF ERA5 Forecast and Reanalysis Data

155 Our TCWV retrieval is based on an inversion technique (Sec. 3) which uses a first guess, as well as a priori and ancillary parameter data. These may come from a climatology or could be set to a global climatological value. However, retrieval

160 performance can be greatly increased and sped up if the a priori data are already slightly closer to the solution. This is why we chose to provide the algorithm with Numerical Weather Prediction (NWP) forecast fields. These were acquired from the European Centre for Medium-Range Weather Forecasts (ECMWF) ERA5 forecasts initialised at 6 UTC and 18 UTC of each day (Hersbach et al., 2020). The ERA5 forecasts are a by-product of the reanalysis and more readily available for past time steps than the operational forecasts. They are different from ECMWF's Integrated Forecasting System (IFS) operational forecasts since they use more assimilated data in the initialisation time step. The forecasts are at a resolution of 0.25° and in 3 h steps. The data fields are interpolated to the observation time and FCI coordinates.

165 The variables needed are: horizontal wind speed (WSP) calculated from u- and v-component of the horizontal wind speed at 10 m above ground (U10, V10), TCWV, surface air temperature at 2 m above ground (T2M), and surface air pressure (SP). The data were accessed via the Copernicus Climate Change (C3S) data store (Copernicus Climate Change Service and Climate Data Store, 2023). For testing and algorithm development, we used the ERA5 forecasts. In the later processing for the NWCSAF GEO software package, the operational ECMWF IFS forecasts at a resolution of 0.5° and 1 h steps will be used.

2.4 Aerosol Optical Thickness Climatology

170 One key parameter for the retrieval of TCWV over water is the aerosol optical thickness (AOT). As a first guess for AOT, we use a climatology at a 1° spatial resolution. It was built from monthly means of the Oxford-RAL Aerosol and Cloud (ORAC, Thomas et al. (2009)) aerosol optical properties data retrieved with Sentinel-3 Sea and Land Surface Temperature Radiometer (SLSTR) and Environmental Satellite (ENVISAT) Advanced Along Track Scanning Radiometer (AATSR) between 2002 and 2022. These data were also accessed via the C3S data store (Copernicus Climate Change Service and Climate Data Store, 175 2019).

2.5 Reference Datasets, Match-up Analysis and Performance Indicators

180 In order to verify the credibility of the retrieved TCWV we need reference data within the field of view of FCI. There are four established sources of TCWV estimates: radiosondes, ground-based GNSS meteorology, ground-based MWR, and ground-based direct sun-photometry. TCWV from NWP Reanalyses may also be used, but their coarse resolution cannot resolve the fine variabilities found in the WV field at the satellite-pixel scale. Reanalyses may be used to assess the stability of the dataset later on. Unfortunately, until the completion of this work, no long-term record of FCI data was available in the final calibration. Because of this, we processed the spectrally representative FCI data discussed above and compared these against TCWV from the ERA5 reanalysis. The performance of our algorithm as well as the accuracy of our calculations, require testing on real data. Hence, we processed a 7-year matchup database of OLCI Level 1b observations and MWR TCWV from the Southern Great 185 Plains site of the Atmospheric Radiation Measurement network (ARM) (Sisterson et al. (2016). Additionally, the set of 1800 OLCI-SLSTR swaths was processed with our algorithm (including the surface reflectance approximation from Sec. 3.4). These were compared against reference TCWV data retrieved at sites of 1) the Aerosol Robotic Network (AERONET) (Holben et al. (1998)), 2) the ARM network (Turner et al. (2007); Cadeddu et al. (2013)) and 3) the SUOMINET network (Ware et al., 2000).

Prior to the analysis, OLCI swaths and ground-based network sites were collocated within 1 km and 30 minutes of a satellite 190 overpass. A square of 11 by 11 pixels around the collocated center pixel was taken into account. Then, these pixels were screened for convergence, a cost-function below 1, and cloud-screened with a buffer of 3 pixels around the cloud mask, minimizing the effect of cloud and cloud shadow contamination. Match-up cases with less than 95% valid pixels were rejected, the central 3 by 3 pixels had to be completely cloud-free.

Both in the assessment of assumptions and the assessment of TCWV quality, we use metrics. Their abbreviations are as 195 follows: N is the number of matchups, MADP is the mean absolute percentage deviation, RMSD is the root mean square deviation, cRMSD is the centered RMSD (i.e., the observation is corrected for the bias against the reference), R^2 is the Pearson correlation coefficient. ODR α and β are the orthogonal distance regression coefficients for the intersect and slope, respectively, with equal weights for all data points.

3 Algorithm Description

200 3.1 Physical Background

The $\rho\sigma\tau$ WV absorption bands are due to the vibrational reaction in a gaseous water molecule hit by a photon within a specific range of wavelengths, see Fig. 1. The absorption of WV in this spectral region is weak compared to the TIR at, e.g., 6.7 or 7.3 μm (traditionally referred to as WV bands). Because of that, the whole column's content of atmospheric WV can be probed using the $\rho\sigma\tau$. While the signal within the absorption band decreases with WV content, an adjacent window band will be 205 virtually unaffected by any change in WV amount along the line-of-sight (LOS). FCI features a "window" band with a nominal center wavelength of $0.865\ \mu\text{m}$ and an "absorption" band with a nominal center wavelength of $0.914\ \mu\text{m}$. The spectral response functions (SRF) are also shown in Fig. 1.

The overall strongest influence factor on the signal measured at the satellite sensor is the surface reflectance. This is also referred to as the surface spectral albedo (ALB) and is the ratio of outgoing irradiance against incoming irradiance at one 210 specific wavelength. This depends on the type of surface covering (e.g., vegetation, sand, snow, etc.) and to some degree on the sun and viewing angles. For land cases the spectral albedo in the NIR is well above 0.3 and thus provides a strong signal relative to the absorption by WV. Over the majority of water surfaces, however, the surface reflectance is often well below 0.03. There is no direct way to measure this spectral albedo, hence an approximation is necessary.

A slightly less important effect comes from scattering aerosol layers below a certain level of aerosol optical thickness (AOT). 215 In that case, the effective LOS is shortened by the higher aerosol layer, and since the humidity content on average is much lower in the higher troposphere, the absorption is decreased substantially. Over bright surfaces, this effect is much less important than over dark surfaces (Lindstrot et al., 2012). Since most natural surfaces over land are bright in the NIR, the shielding effect of an average aerosol layer is small (Diedrich et al., 2015).

Under most circumstances, this assumption is not valid for water surfaces, though. Due to the low albedo, already slightly 220 scattering layers of aerosol may create the effect described above. To a certain degree, this effect can be corrected for by simulating an aerosol layer with a specific AOT in the algorithm. However, for this, the effective height of the aerosol layer

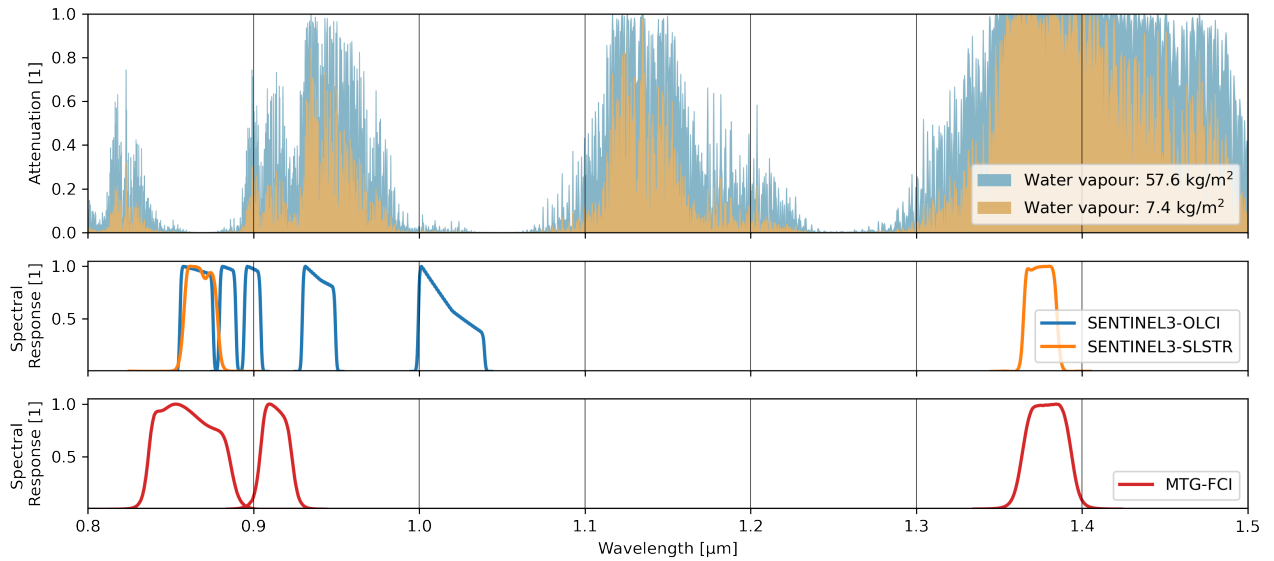


Figure 1. Upper panel: The WV attenuation spectrum for an atmosphere with a low TCWV amount in orange (7.4 kg/m^2) and high TCWV amount in blue (57.6 kg/m^2) with data obtained from the Correlated K-Distribution Model Intercomparison Project (CKDMIP, Hogan and Matricardi (2020)). Center panel: The SRFs in the NIR part of the spectrum for the satellite instruments OLCI (blue) and SLSTR (orange). Lower panel: the SRFs in the NIR for FCI (red).

needs to be estimated which is a challenge in and of itself. Another important aspect over water surfaces is sunglint, i.e., the reflectance's dependency on wind-speed and viewing/solar geometry. High wind speeds create a rough surface with low reflectance peaks spread out over a range of observation geometry angles. At lower wind speeds, a calm surface results in a higher reflectance peak over a limited range of observation angles, similar to a mirror. In regions with strong sunglint, the relative influence of aerosol scattering is reduced.

225

Over both land and water surfaces, the atmospheric temperature profile and surface pressure play a lesser role due to temperature- and pressure-dependent line broadening (Rothman et al., 1998). For more detail, see In contrast to TCWV retrievals in the TIR, the impact of the temperature profile is substantially lower but not negligible. The uncertainties due to a mis-characterised temperature profile are approximately 0.6 kg/m^2 and surface pressure at about 0.9 kg/m^2 (Lindstrot et al., 230 2012).

3.2 Forward Model

The first step in our framework is to run radiative transfer simulations (RTS) for a set of complete and comprehensive atmospheric, surface and geometric conditions as described in the previous section and summarised in Table 1 and 2. For the 235 simulation of top-of-atmosphere (TOA) reflectances we used the Matrix Operator Model (MOMo, Fell and Fischer (2001);

Variable Name	Increments and units
TCWV	0.1, 1.0, 5.0, 10., 25., 50., 75.0 kg/m ²
ALB	0, 0.1, 0.3, 0.6, 1
T2M	standard atmospheric profiles 1 to 5*
SP	500, 650, 750, 850, 950, 1050 hPa
SUNZ	0, 10, 20, 30, 40, 50, 60, 70, 80, 90°
SATZ	0, 10, 20, 30, 40, 50, 60, 70, 80, 85°
RAZI	0, 18, 36, 54, 72, 90, 108, 126, 144, 162, 180°

Table 1. Land Surface Setup for MOMo. *Standard profiles from Anderson et al. (1986).

Variable name	Range and units
TCWV	0.1, 1.0, 5.0, 10., 25., 50., 75.0 kg/m ²
AOT	0.001, 0.1, 0.3, 0.5, 0.7, 1.2 at 700 to 1000 m height
WSP	2, 3, 5, 10, 15 m/s
T2M	standard atmospheric profiles 1 to 5*
SP	950, 1000, 1050 hPa
SUNZ	0, 10, 20, 30, 40, 50, 60, 70, 80, 90°
SATZ	0, 10, 20, 30, 40, 50, 60, 70, 80, 85°
RAZI	0, 18, 36, 54, 72, 90, 108, 126, 144, 162, 180°

Table 2. Water Surface Setup for MOMo. *Standard profiles from Anderson et al. (1986).

Hollstein and Fischer (2012); Doppler et al. (2014)). These simulations are finally sorted into two land look-up-tables (LUT) for land surfaces and water surfaces, respectively.

Over land surfaces, the surface albedo (ALB) is defined as isotropic. Over water surfaces, the surface reflectance is estimated from the 10 m wind speed (WSP) using Cox and Munk (1954). Standard atmospheric profiles were taken and adapted from

240 Anderson et al. (1986) to provide the vertical distribution of temperature and humidity. The numbers refer to: 1. mid-latitude summer, 2. mid-latitude winter, 3. sub-Arctic summer, 4. sub-Arctic winter, 5. tropical. Based on the forecast surface air temperature (T2M) and surface pressure (SP) the associated atmospheric profile group is chosen. The humidity profiles are scaled with TCWV. All simulations are done for a set of satellite zenith angles (SATZ), sun zenith angles (SUNZ) and relative azimuth (RAZI). RAZI is calculated from the satellite azimuth angle (SATA) and sun azimuth angle (SUNA) following:

245
$$RAZI = \arccos(\cos(SUNA) * \cos(SATA) + \sin(SUNA) * \sin(SATA)) \quad (1)$$

The aerosol mixtures and their optical properties have been calculated using the OPAC software package (Optical Properties of Aerosols and Clouds, Hess et al. (1998)). Within their documentation you can find details on the used aerosol mixtures for the two types chosen for the land and water surface simulations. Over land we used the aerosol mixture "continental average", over ocean we used the aerosol mixture "maritime clean". In both cases, we simulated a homogenous aerosol layer between

250 700 to 1000 m height above ground with the specified AOT. An overview of the inputs and increments used for the simulations is shown in Tables 1 and 2.

The observations we simulate are the normalised radiance in the window channel ($nL_{TOA}(0.865\mu m)$) and the pseudo optical thickness in the absorption channel ($\tau_{pTOA}(0.914\mu m)$). The normalised radiance is calculated as follows:

$$nL_{TOA}(\lambda) = \frac{L_{TOA}(\lambda)}{F_0(\lambda)} \quad (2)$$

255 where F_0 is the spectral solar irradiance.

The pseudo optical thickness τ_{pTOA} is calculated as follows:

$$\tau_{pTOA}(\lambda) = -a - \frac{\log\left(\frac{nL_{TOA}(\lambda)}{nL_{TOA}^*(\lambda)}\right)}{\sqrt{AMF}} \cdot b \quad (3)$$

where AMF is the air mass factor, nL_{TOA}^* is the normalised radiance corrected for the influence of WV absorption, a and b are the so-called correction coefficients which may correct for a systematic bias discovered in a validation against reference 260 TCWV observations.

The AMF is calculated as follows:

$$AMF = \frac{1}{\cos(SUNZ)} + \frac{1}{\cos(SATZ)} \quad (4)$$

Dividing through \sqrt{AMF} , the relationship between TCWV and τ_{pTOA} becomes more linear, reducing the number of necessary iterations in the inversion later on. nL_{TOA}^* needs to be approximated using other available information (e.g., a 265 climatology atlas, neighbouring window channels). Here, we use a more elaborate technique, described in Subsection 3.4.

Preusker et al. (2021) have obtained the correction coefficients a and b by minimizing the differences between simulated and measured OLCI observations using ARM-SGP.C1-MWR TCWV as an input (see Preusker et al. (2021) for details). For OLCI's version of this algorithm, a and b for band 19 (at 0.9 μm) were estimated to be -0.008 and 0.984, respectively, from the results shown in Sec. 4.1. For FCI, other MWR TCWV references will be necessary. We intend to use reference sites such 270 as Meteorological Observatory Lindenberg – Richard Assmann Observatory (MOL–RAO) (Knist et al., 2022), the Cabauw Experimental Site for Atmospheric Research (CESAR) (Van Ulden and Wieringa, 1996) or ARM — Eastern North Atlantic (ENA) (Mather and Voyles, 2013).

The set of simulations is sorted into a multi-dimensional look-up table (LUT). This LUT can then be used to simulate a measurement (\mathbf{y}) for a given set of states (\mathbf{x}) and parameters (\mathbf{p}) using an interpolator. This is referred to as the forward model 275 \mathbf{F} . With this forward model, we can estimate a sensor's observation for a given set of states as follows:

$$\mathbf{y} = \mathbf{F}(\mathbf{x}, \mathbf{p}) + \epsilon \quad (5)$$

ϵ denotes the measurement and forward model error. The state vector of land consists of TCWV and ALB(0.865 μm), over water surfaces it consists of TCWV, WSP, and AOT. The parameter vector is composed of T2M, SP, SUNZ, SATZ and RAZI.

3.3 Inversion Using Optimal Estimation

280 Eq. 5 can be inverted to retrieve a state associated with an observation. There are various ways of performing this inversion. We chose to follow the optimal estimation (OE) approach for atmospheric inverse problems described by Rodgers (2000). In essence, this inversion is based on the principle of minimizing the cost function \mathbf{J} by iteratively changing the initial first guess of a state or the state of the prior iteration step.

The iterative process is stopped if either the maximum number of allowed steps is reached or the following criterion is met 285 by the retrieved state \mathbf{x}_{i+1} :

$$(\mathbf{x}_i - \mathbf{x}_{i+1})^T \hat{\mathbf{S}}_i^{-1} (\mathbf{x}_i - \mathbf{x}_{i+1}) \leq n \cdot \epsilon \quad (6)$$

where $\hat{\mathbf{S}}$ is the retrieval error-covariance, n is the number of state variables. More details on the process of OE within a TCWV retrieval framework can be found in Preusker et al. (2021) and El Kassar et al. (2021). One crucial advantage of OE is the simultaneous retrieval of the associated uncertainty, the so-called retrieval error covariance matrix $\hat{\mathbf{S}}$.

290
$$\hat{\mathbf{S}} = (\mathbf{S}_a^{-1} + \mathbf{K}_i^T \cdot \mathbf{S}_\epsilon^{-1} \cdot \mathbf{K}_i)^{-1} \quad (7)$$

Where, \mathbf{S}_a is the a priori error covariance matrix associated with \mathbf{x}_a , \mathbf{S}_ϵ is the measurement error covariance matrix associated with \mathbf{y} and \mathbf{K} is the Jacobian which contains the partial derivatives of each measurement to each state at step i (i.e., $\mathbf{K}_i = \partial \mathbf{F}(\mathbf{x}_i) / \partial \mathbf{x}_i$). The covariances may either be set to values that correspond to the actual covariances within a given variable. However, the covariances may also be used as tuning parameters in order to make the algorithm lean more towards the measurement or more towards the prior knowledge Rodgers (2000). Over land surfaces we set the a priori uncertainty of TCWV very high (16 kg/m^2) since the information content of the absorption band is high over bright surfaces. Over the ocean, the TCWV a priori uncertainty was set much lower (2.5 kg/m^2). The ALB a priori uncertainty is set to 0.5, the WSP a priori uncertainty is set to 5 m/s , the AOT a priori uncertainty is set to 0.55. The corresponding covariances are the squared uncertainties.

300 The error covariance of τ_{pTOA} is estimated using the signal-to-noise-ratio (SNR), an interpolation-error (ϵ_{intp}),from the uncertainty in estimating nL_{TOA}^*) and AMF:

$$\mathbf{S}_\epsilon(\tau_{pTOA}) = \left(\frac{1}{SNR^2} + \frac{1}{SNR^2 + \epsilon_{intp}} \right) \cdot \frac{1}{AMF} \quad (8)$$

In 8, the two SNR-terms refer to the uncertainty of $nL_{TOA}(0.914)$ and $nL_{TOA}^*(0.914)$. For $nL_{TOA}(0.865\mu\text{m})$ the error covariance is simply $\frac{1}{SNR^2}$.

305 An additional metric this inversion technique provides is the so-called averaging kernel \mathbf{A} :

$$\mathbf{A} = \mathbf{G} \cdot \mathbf{K} = \frac{\partial \hat{\mathbf{x}}}{\partial \mathbf{x}} \quad (9)$$

where \mathbf{G} is the Gain matrix, which contains the partial derivative of the true state $\partial \hat{\mathbf{x}}$ in relation to the partial derivative of the measurement $\partial \mathbf{y}$. While the true state $\hat{\mathbf{x}}$ is unknown, the relative changes at each step quantify the sensitivity of $\hat{\mathbf{x}}$ towards changes in \mathbf{y} .

310 The entries along the diagonal of \mathbf{A} correspond to the state variables and show a range of values between 0 and 1. At 0, the proportion of the retrieved state to $\hat{\mathbf{x}}$ is lowest; the measurement did not contribute to the retrieval. At 1, the proportion of the retrieved state to the true state is highest. Everything in between indicates that some improvement of the prior information about the state could be made using the measurement. The trace of AVK gives the degrees of freedom of the measurements.

3.4 Estimation of nL_{TOA}^* with Principle Component Regression

315 For some surfaces (e.g., calm, clear water), the difference in spectral albedo between the window and absorption channel is small. Over most other surfaces, however, this is not the case. Simply using $nL_{TOA}(0.865\mu\text{m})$ for nL_{TOA}^* would yield an unreliable estimate of the pseudo optical depth τ_{pTOA} . Thus, in order to calculate τ_{pTOA} we need an accurate estimate of

the spectral slope between the window and the absorption channel. For satellite sensors such as MODIS or OLCI, the WV absorption bands have at least two accompanying window bands (i.e. at 0.865, 0.885, 1.02 or 1.2 μm). FCI and other future instruments do not have such additional window channels close by. Hence, another technique to estimate the spectral slope is needed. The principal component regression (PCR) facilitates the reconstruction of a continuous set of observations from few discrete data points. This approach is already used with reasonable success in the estimation of BRDFs and reflectance spectra within RTTOV (Vidot and Borbás, 2014). Their approach was used as a blueprint for our spectral slope estimation.

The ECOSTRESS spectral library version 1.0 provided by the United States of America Geological Service (USGS) is a collection of spectral reflectances for individual materials and/or mixtures at a high spectral resolution (Meerdink et al., 2019). The library consists of spectra for a wide range of material groups: human-made, rock, soil, mineral, photosynthetic vegetation, non-photosynthetic vegetation, water (which includes fresh-water, ice, and snow). A small selection of these spectra is depicted in the upper part of Fig. 2, below, the SRFs of a selection of sensors are shown.

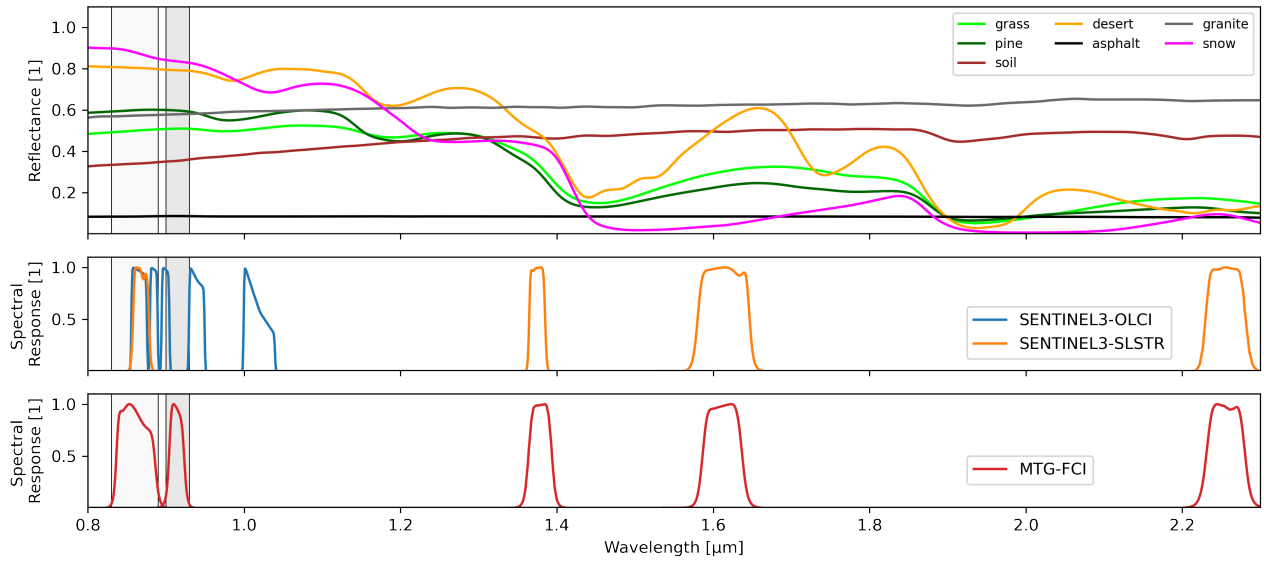


Figure 2. Upper panel: overview of a selection of surface reflectance spectra from Meerdink et al. (2019), the labels are representative and not the actual spectra designations. Central panel: the SRFs of OLCI (blue) and SLSTR (orange). Lower panel: the SRFs of FCI (red).

Only spectra between 0.4 and 2.35 μm were taken into account and linearly interpolated to a spectral resolution of 0.001 μm . To avoid a sampling bias towards a specific group of spectra, we used similarly sized subsets of each category. From this 330 database, the principal components (the Eigenvectors, PCs) are calculated and sorted by their associated Eigenvalue. Instead of reconstructing spectrally high-resolved reflectances, we use the PCs to reconstruct the reflectance of two channels: at 0.865 μm and at 0.914 μm referred to as the *target*. Following the nomenclature of Vidot and Borbás (2014), $\mathbf{R}_{\text{target}}$ is the vector of reflectance spectra folded to the target SRFs, \mathbf{c}_{win} is the regression coefficient vector (also referred to as weights) from

335 the window bands and \mathbf{U}_{target} is the matrix of the selected PCs of the high-resolution reflectance spectra, folded to the target SRFs.

$$\mathbf{R}_{target} = \mathbf{c}_{win} \mathbf{U}_{target} \quad (10)$$

Using the Moore-Penrose Pseudo inverse, the regression coefficient \mathbf{c}_{win} follows:

$$\mathbf{c}_{win} = \mathbf{R}_{win} \mathbf{U}_{win}^T (\mathbf{U}_{win} \mathbf{U}_{win}^T)^{-1} \quad (11)$$

340 An optimal configuration of the number of PCs and bands was then found by comparing different band combinations with several numbers of PCs. For this, we reconstructed all available spectra (which were used in the PCR) at the target bands from the folded spectra at the window bands. Using this approach, the optimal configuration for FCI was found with the use of five window bands (i.e., negligible WV attenuation) in the VIS to SWIR (0.51, 0.64, 0.865, 1.61, 2.25 μm) and only the first four PCs. We are able to reproduce the actual surface reflectance at the absorption and window band with a bias of 0.0045 and 345 0.0038 and a RMSD of 0.016 and 0.02, respectively. Folding the PCs to the SRFs of other sensors would make this matrix applicable to other instruments with similar bands, as shown in Fig. 2. In order to estimate the spectral slope in the PCR, FCI's normalised radiances at the window channels need to be transformed into irradiance reflectances:

$$\rho_{TOA}(\lambda) = \frac{nL_{TOA}(\lambda) \cdot \pi}{\cos(SUNZ)} \quad (12)$$

From the reconstructed surface reflectances we calculate the slope r :

$$350 \quad r = \frac{\rho(0.914)}{\rho(0.865)} \quad (13)$$

This ratio is then multiplied with the $nL_{TOA}(0.865\mu\text{m})$ in order to yield a more accurate estimate of nL_{TOA}^* at the absorption band. The underlying assumption is that between 0.865 and 0.914 μm , atmospheric scattering and attenuation other than WV are nearly identical. Thus $\frac{ALB(0.914)}{ALB(0.865)} \approx \frac{\rho_{TOA}(0.914)}{\rho_{TOA}(0.865)}$ holds true. Given a sufficiently bright surface and outside of the influence of thick, scattering layers (e.g., clouds, aerosols) or outside of very slant viewing geometries ($SATZ > 82^\circ$), this is the case. 355 Over water surfaces, the influence of scattering processes in the atmosphere is much stronger. Hence, the uncertainties over water pixels are higher. Furthermore, the influence of water constituents (e.g., sediment, pigments) on the water reflectance spectrum in the NIR has not been taken into consideration. The PCA training dataset almost exclusively consisted of terrestrial reflectances and only a few fresh water reflectances.

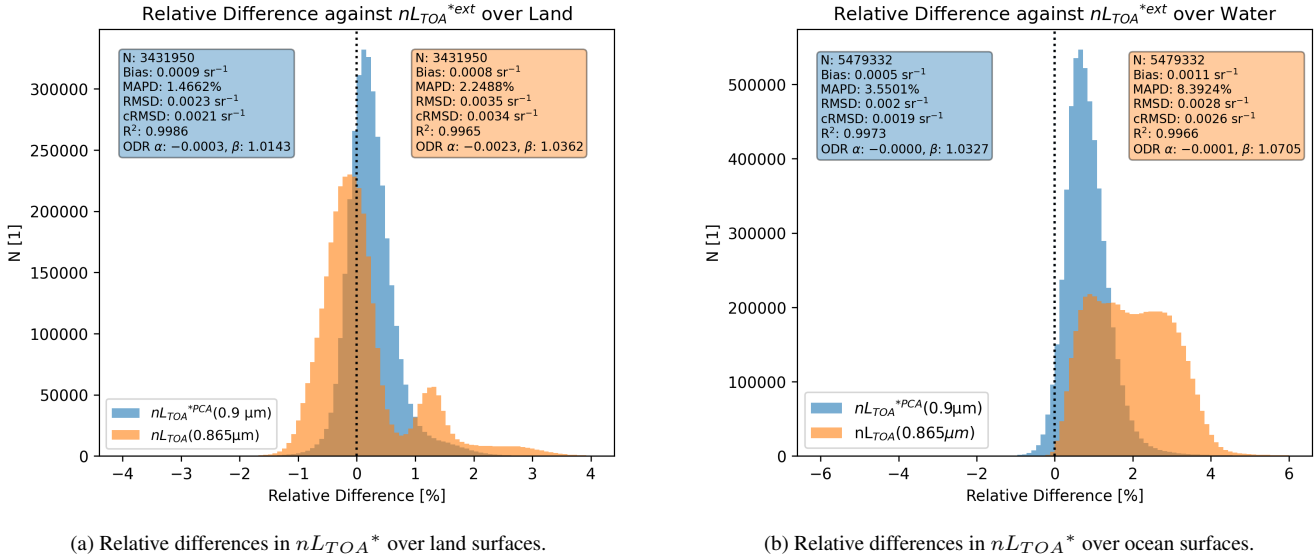


Figure 3. Relative differences between two proposed nL_{TOA}^* against the extrapolated nL_{TOA}^{*ext} as used in the COWa algorithm over land and water surfaces, respectively. The associated metrics in the corresponding colours are found in the top corners. The solid black line indicates 0% relative deviation.

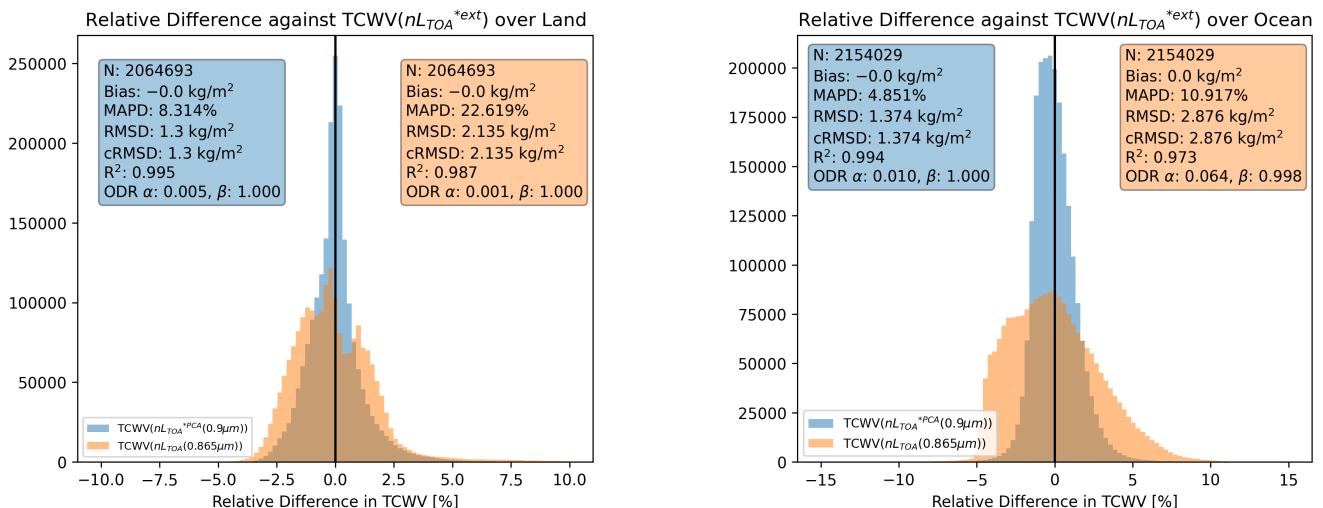
Using the OLCI/SLSTR synergy allows us to assess the performance of the PCR to estimate τ_{pTOA} in comparison to directly 360 using the window ($nL_{TOA}(0.865 \mu\text{m})$) against a common reference. In the Copernicus Sentinel-3 OLCI Water Vapour product (COWa) algorithm, $nL_{TOA}^*(0.9 \mu\text{m})$ is extrapolated from the two adjacent window bands at 0.865 and 0.885 μm (Preusker et al., 2021). For $\tau_{pTOA}(0.94\mu\text{m})$, $nL_{TOA}^*(0.94 \mu\text{m})$ is interpolated from the two window bands 0.885 μm and 1.020 μm . This is substantially closer to the "real" surface reflectance than using the PCR. Hence, we compare $nL_{TOA}^{*PCA}(0.9 \mu\text{m})$ 365 against $nL_{TOA}^{*ext}(0.9 \mu\text{m})$ from the extrapolation using the two adjacent window channels. For this and other comparisons, we calculated the relative difference in % by dividing the absolute difference (observation minus reference) by the reference multiplied by the factor 100. Fig. 3a and 3b reveal that the vast majority of points lie close to 0 % line for both land and water pixels, albeit with a positive bias. In contrast, using the 0.865 μm normalised radiance by itself would yield much worse results. I.e., a strong bi-modal distribution over land and a weaker bi-modal distribution with a wide spread over water (see Fig. 3a and 3b).

370 On average, there is a small positive bias in $nL_{TOA}^{*PCA}(0.9 \mu\text{m})$ both over land (+0.3%) and water (+0.8%). Over land pixels, the 98th percentile of the relative percentage deviation is 1.7% against the 2.6% when using $nL_{TOA}(0.865 \mu\text{m})$ as nL_{TOA}^* . Over water pixels, the 98th percentile of the relative percentage deviation lies at 2.2%, whereas this value is 4% when using $nL_{TOA}(0.865\mu\text{m})$ as nL_{TOA}^* . On average, an increase of 1% in $nL_{TOA}^*(0.9 \mu\text{m})$ roughly translates to a 1.6% increase (approx. 0.9 kg/m^2) of TCWV estimate. A correction of this bias may be possible, but since such an analysis cannot 375 be carried out using FCI, we decided against it. Because the PCR performed better than the window channel by itself, we

decided to use $nL_{TOA}^{*PCR}(0.9 \mu\text{m})$ to calculate τ_{pTOA} over both land and water surfaces. Despite the slight deviations, the PCR approach remains a good technique in order to reduce the impact of the spectral slope as much as possible.

This can also be demonstrated using a TCWV processed from a single day of OLCI/SLSTR observations. Here, we compared the retrievals from using each nL_{TOA}^{*ext} , nL_{TOA}^{*PCR} , and $nL_{TOA}(0.865 \mu\text{m})$ to calculate τ_{pTOA} as input to the algorithm.

380 In order to only see the influence on precision of TCWV, both datasets have been bias-corrected. The results are shown in Fig. 4. Over land surfaces, the bi-modal distribution in using $nL_{TOA}(0.865 \mu\text{m})$ persists with large spread and systematic over- and under-estimations. Over the ocean, the difference between the two approaches is even more pronounced. Both MAPD and RMSD indicate that using nL_{TOA}^{*PCR} instead of $nL_{TOA}(0.865 \mu\text{m})$ for the calculation of τ_{pTOA} improves the retrieval substantially.



(a) TCWV using nL_{TOA}^{*PCR} from the PCR against the extrapolated $nL_{TOA}^{*}(0.9 \mu\text{m})$ over land pixels for a random subset of data in June 2021.

(b) Relative difference against $nL_{TOA}^{*}(0.9 \mu\text{m})$ from the PCR against the extrapolated $nL_{TOA}^{*}(0.9 \mu\text{m})$ over water pixels for a random subset of all data in June 2021.

Figure 4. Relative difference between TCWV retrieved with τ_{pTOA} calculated from extrapolated nL_{TOA}^{*ext} and nL_{TOA}^{*PCR} from the PCR in blue and τ_{pTOA} calculated from $nL_{TOA}(0.865 \mu\text{m})$ in orange. The TCWV has been bias-corrected against the reference (TCWV using nL_{TOA}^{*ext}). The data are for a random subset of one day in June 2021. The associated metrics in the corresponding colours are found in the top corners. The solid black line indicates 0% relative deviation.

385 In very rare cases (<0.1%), there are large deviations (>5%). Upon visual inspection, these extreme deviations mostly occur along rivers, coasts, in high elevations or at the poles. We assign these cases to 1) unidentified clouds, 2) coastal and inland water pixels with mixed contributions by land and water, 3) water-constituents changing the NIR reflectance of the water surface substantially, 4) adjacency effects, the brightening effect of dark pixels by diffuse radiation from neighbouring bright pixels and 5) geolocation and unphysical spectral matches between OLCI and SLSTR. Yet, these rare deviations are still lower 390 than the extreme deviations found by using the window band at 0.865 μm itself.

3.5 Finalised Retrieval Framework

The retrieval procedure is as follows. FCI (or OLCI/SLSTR) radiometric and ancillary data are read and the necessary auxiliary fields (ECMWF forecast, AOT) are interpolated to satellite resolution. In the next step, the cloud mask and the measurements (e.g. reflectances, τ_{pTOA} , etc.) are calculated. A land and water processing mask is made. Pixels which are marked as cloudy or where $SUNZ$ is too slant ($> 80^\circ$) are filtered out.

The inversion is run up until a pre-defined convergence criterion. Once this is reached, this state is passed out of the algorithm and these pixels are marked as converged. If the maximum allowed number of iterations is exceeded (6 over land, 8 over ocean), the algorithm stops, and these pixels are marked as not-converged. Furthermore, the estimate of the associated uncertainty in the retrieved state is provided as part of the algorithm's output.

After the processing has finished for all pixels, data are only marked as valid if their cost is below a threshold (currently < 1) and if the convergence criterion has been met. With this, some cloudy pixels which have been missed by the cloud mask or pixels containing a thick and/or elevated aerosol layer may be filtered out. This is due to the fact that NIR-TCWV retrievals in the presence of elevated cloud or aerosol layers often lead to a substantial underestimation of TCWV, compared to the TCWV found in the prior/first guess. This leads to the cost function becoming extremely high.

405 4 Results

4.1 Sentinel3 OLCI and OLCI/SLSTR data

An initial test for our forward model as well as the inversion technique, was the application to an existing matchup database used for the validation and quality control of COWa. OLCI measurements were spatio-temporally collocated with the ARM network site Southern Great Plains (SGP) positioned in the Midwest of the United States of America (USA). The dataset is limited to one location only and runs from 2016 to 2023. Since SLSTR measurements are missing from this dataset, the approximation of $nL_{TOA} * PCR$ in the absorption band using the PCA regression could not be done. Instead, we choose the same approach as COWa: extrapolate nL_{TOA} from band 17 (0.865 μm) and band 18 (0.885 μm) to band 19 (0.9 μm).

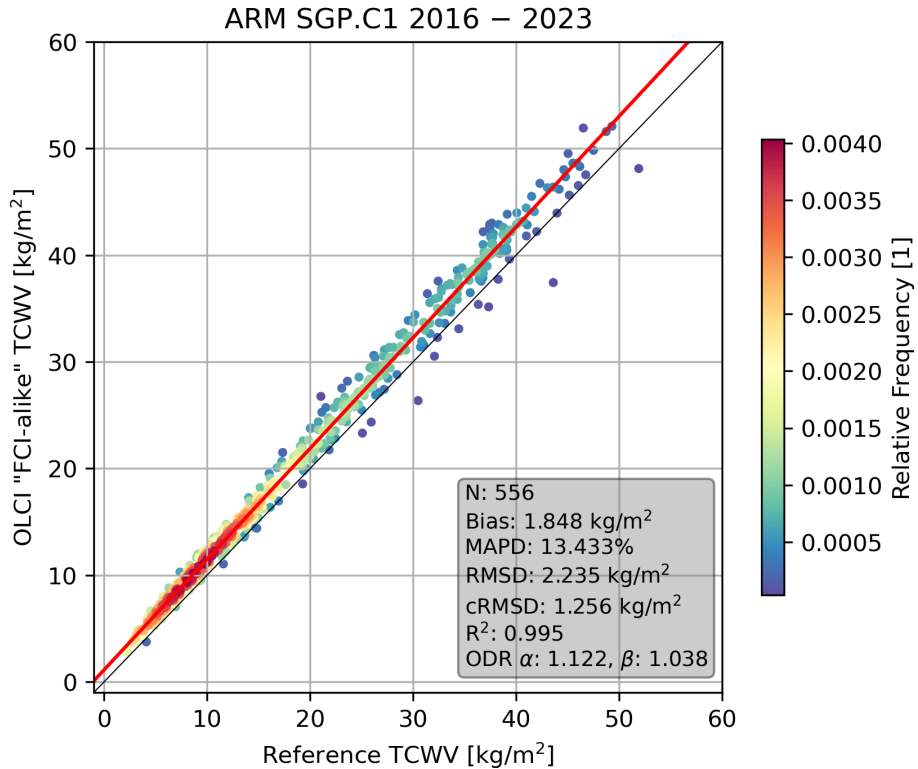


Figure 5. Comparison of S3OLCI "FCI-like" TCWV (using nL_{TOA}^{ext}) against ARM TCWV at the SGP site, coloured with the relative frequency of occurrence. The solid black line presents the 1:1 line, the red line marks the ODR curve.

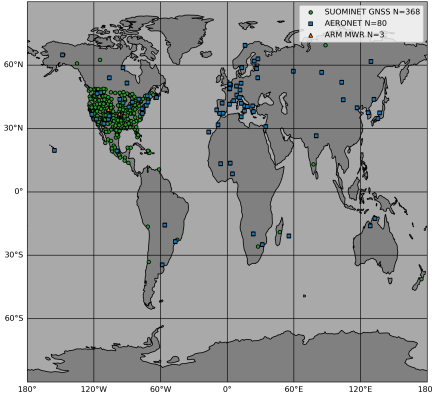
The analysis of the two-band OLCI TCWV yields a strong correlation with a Pearson correlation coefficient of 0.995. The bias of 1.848 kg/m², orthogonal distance regression (ODR) coefficients, i.e., offset (α) and slope (β) of 1.122 and 1.038, respectively, indicate a slight wet bias. The cRMSE of 1.256 kg/m², RMSD of 2.235 kg/m² and MAPD of 13.433% still indicate slight spread.

In a next step, we processed the global dataset of the OLCI-SLSTR synergy. This has been done in order to assess the quality of the two-band approach and the LUT-inversion in combination with the PCR approach to estimate $\tau_{pTOA}(0.9 \mu\text{m})$.

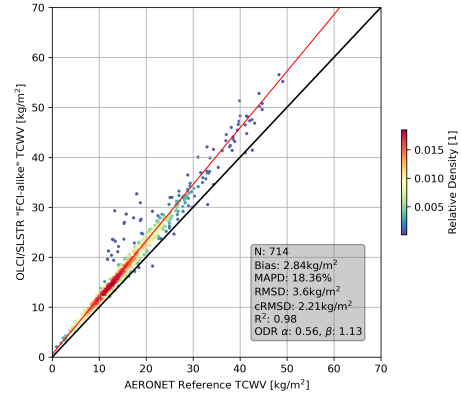
This TCWV was compared against three different reference networks. For this matchup analysis, we followed the same matchup procedure as before. The results of the comparisons are depicted in Fig. 6a to 6d. Fig. 6a shows the positions of the ground-based reference sites with at least one valid matchup according to their network. For the ARM network, only 3 stations in North America were available for 2021. With AERONET and SUOMINET, a wider range of different climate zones and atmospheric conditions can be covered. The comparison of 714 valid matchups against 80 AERONET stations in Fig. 6b reveals a wet bias of 2.84 kg/m², a MAPD of 18.36%, a RMSD of 3.6 kg/m², cRMSE of 2.21 kg/m², R^2 of 0.98, and ODR offset and slope of 0.56 and 1.13, respectively. The analysis results for 45 valid matchups against ARM MWR observations can be seen in Fig. 6c and show a slight wet bias of 0.33 kg/m², a MAPD of 6.64 %, a RMSD of 1.49 kg/m², a cRMSE of

1.46 kg/m², R^2 of 0.99, and ODR offset and slope of 0.33 and 1, respectively. In the comparison of 5439 matchups against 368 SUOMININET stations, we find a wet bias of 1.38 kg/m², a MAPD of 16.03 %, a RMSD of 2.22 kg/m², a cRMSD of 1.75 kg/m², a R^2 of 0.98, and ODR offset and slope of 0.65 and 1.04, respectively. Most SUOMINET stations are positioned in

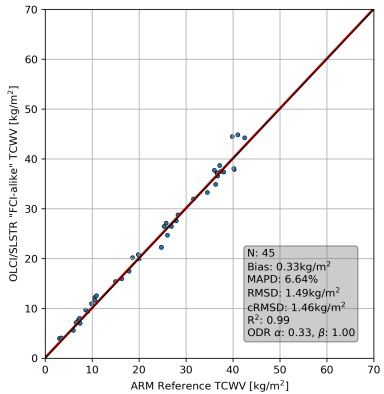
430 Central and North America.



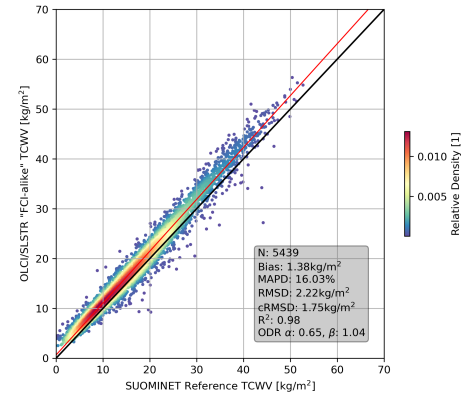
(a) Geographical distribution and their sum of all reference sites from which reference TCWV datasets are used in the matchup analysis.



(b) Comparison of OLCI/SLSTR "FCI-like" TCWV against AERONET TCWV, coloured with the relative frequency of occurrence.



(c) Comparison of OLCI/SLSTR "FCI-like" TCWV against ARM at SGP.C1 TCWV.



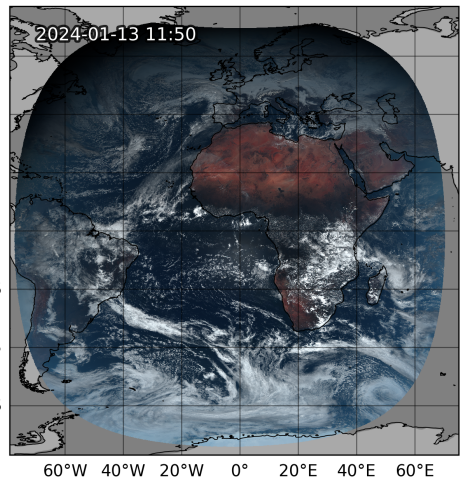
(d) Comparison of OLCI/SLSTR "FCI-like" TCWV against SUOMINET TCWV, coloured with the relative frequency of occurrence.

Figure 6. Matchup Analysis of OLCI/SLSTR "FCI-like" TCWV against globally distributed reference sites. This TCWV uses the PCR approach to estimate τ_{pTOA} . The solid black lines present the 1:1 line, and the red lines mark the respective ODR curves.

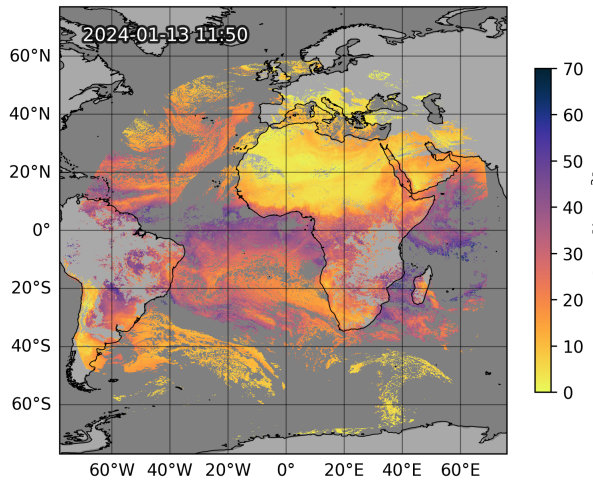
4.2 MTG-FCI Data

In order to test our algorithm with regard to future nominal FCI data, we applied the first prototype on test data provided by EUMETSAT. Since this dataset is still preliminary, this is neither a definitive nor quantitative assessment. Rather, it serves to

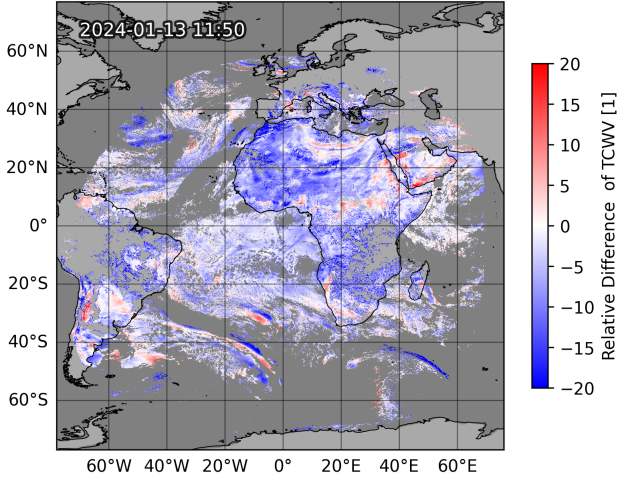
check the processor's performance with real data and check the product for any unexpected behaviour and/or defects. The data
435 were gathered on the 13th of January 2024 at 11:50 UTC. The full-disk true colour RGB and processed TCWV are depicted in
Fig. 7a and 7b, respectively.



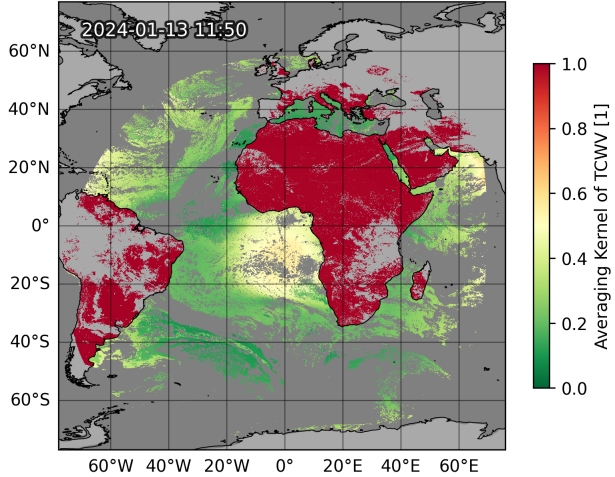
(a) FCI true colour composite.



(b) Retrieved FCI TCWV field.



(c) Relative difference between FCI TCWV and ERA5 reanalysis TCWV.



(d) AVK corresponding to the retrieved TCWV.

Figure 7. Fulldisk visualisation of TCWV and related products, processed from FCI data acquired on 13 January 2024. Dark grey marks land surfaces, light grey marks water surfaces.

In parallel processing, the running time of one full-disk scene on a workstation with 64 GBs of RAM and a 12 core CPU lies below 5 minutes. In single processing, the running time of a single chunk takes about 30 to 50 seconds. This includes input/output operations, cloud-masking, PCR, and inversion.

440 We can see lower TCWV values over mid to high latitudes and higher TCWV amounts all around the ITCZ in Fig. 7b. Arid regions such as the Sahara or the Arabian Peninsula are clearly visible. Europe also exhibits low TCWV. Synoptic features such as bands of elevated moisture are visible. Despite the wide range of viewing zenith and solar zenith angles and their implications for the line of sight, there appears to be no influence on the TCWV product. Over Central Africa, some clouds that are visible in the RGB have not been detected by the cloud mask. Such areas are also distinguishable by their decreased
445 TCWV values compared to the surrounding areas. This underestimation due to clouds as well as the finer details can be seen in a close-up of the scene in Fig. 8b. Because of the 1 km resolution of FCI's NIR channels, we can also detect meso- to mini-scale features such as smaller pockets of high moisture over the ITCZ or the mixing between dry and moist air masses. Closer to the shore, the TCWV field shows slight discontinuities between the water and land surface. The water-pixels close to the shoreline often show values which deviate a few percent from the adjacent land-pixels; in most cases, there is an over-estimation.

450 At this stage, a rigorous quantitative validation of the TCWV product is not feasible, and our comparison against TCWV from the ERA5 reanalysis is not meant as such. As a preliminary way to check the TCWV field for consistency, we plotted the relative difference between the FCI TCWV and a collocated ECMWF ERA5 reanalysis TCWV, shown in Fig. 7c. This gives us a first impression if any artifacts or defects appear or if the algorithm works as intended. The image in Fig. 7c is dominated by negative differences, which translates to a dry bias against the reanalysis TCWV. On average, FCI TCWV is approximately
455 10% drier than the reanalysis over land surfaces and 5% drier over water surfaces. Furthermore, there are areas with positive and negative differences close to one another, often resembling a line, e.g., over Northern Africa or over the South Atlantic. Fig. 7d depicts the AVK at each pixel. Over land, the value is close to 1 for most pixels since the forward model is very sensitive towards changes in the measurements. Over water, this value lies between 0 and 0.7. In areas of sunglint, the AVK ranges between 0.4 to 0.7. In areas with low water-surface reflectance, the AVK approaches 0. In areas with increased AMF and/or
460 TCWV, the AVK is slightly higher between 0.1 to 0.3.

To showcase FCI's spatial resolution, we compare a TCWV field from Sentinel3-A OLCI/SLSTR with real preliminary calibrated FCI from the 27th June 2023 in Fig. 8. Both are processed with the algorithm described above. The temporal difference between the two fields is approximately 5 minutes. The scene is situated in northern Mali in West Africa. The differences in viewing geometry are visible between FCI and OLCI. In the true colour RGB of FCI, longer cloud shadows
465 are visible, which are much smaller in the S3A-OLCI image, or their positions are shifted. The TCWV fields reveal a moist air mass in the South-East, while a drier air mass is positioned in the North-West. Consistent with the comparison against the ERA5 analysis, FCI TCWV is about 10% lower than OLCI TCWV. Hence, another colourmap-range is used in the FCI TCWV image(8b).

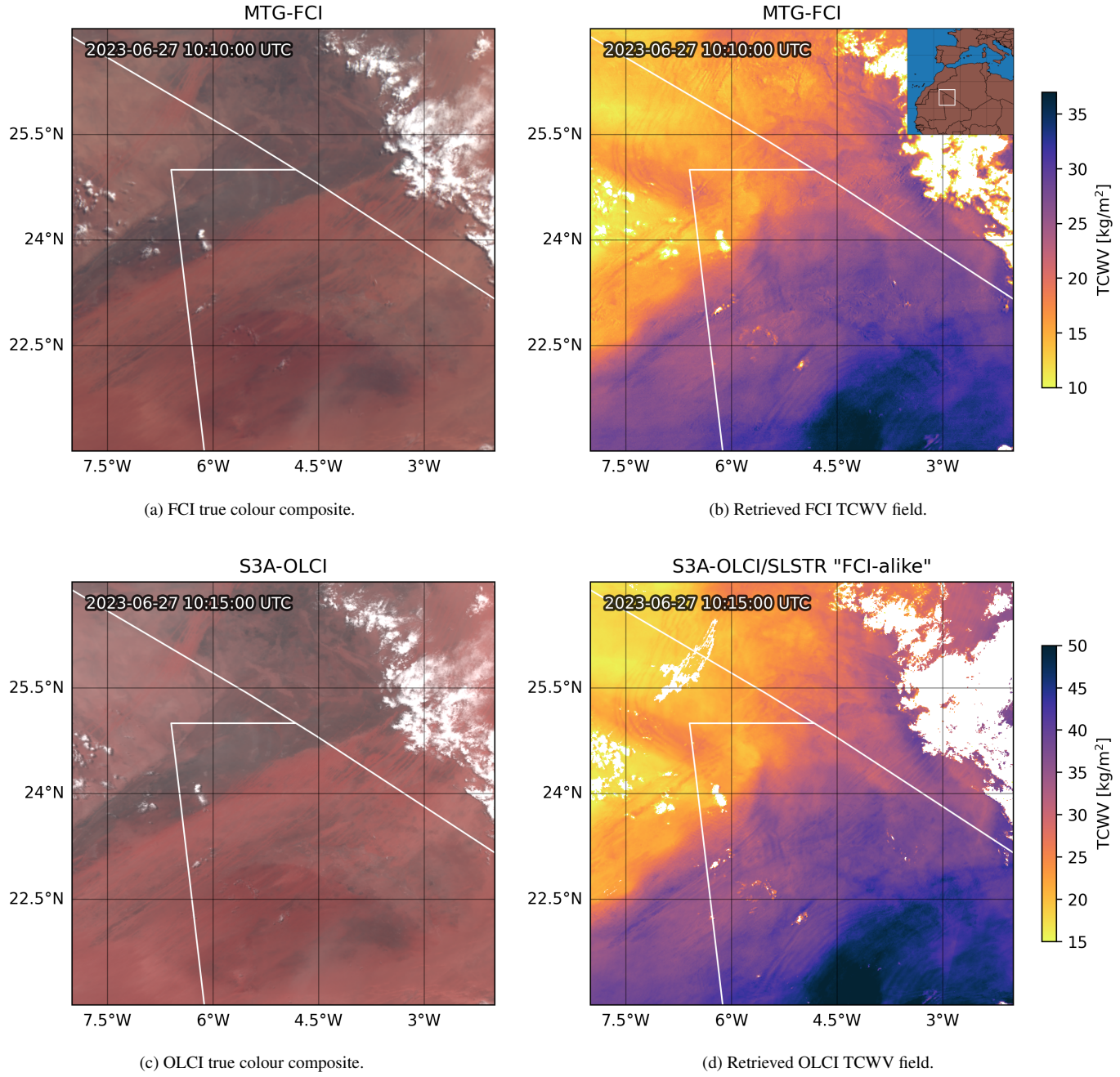


Figure 8. Comparison of FCI TCWV and OLCI/SLSTR "FCI-like" TCWV for a close-up on 27 June 2023 over Northern Mali.

FCI is capable of reproducing the amount of detail found in the OLCI TCWV field: e.g., a dry line in the western half of the 470 image (i.e., strong gradients in moisture between the air masses) or gravity waves in the southern half or north-eastern corner (local, wave-like peaks and troughs in TCWV). The positioning of features appears to be coherent between the two sensors.

Furthermore, we can see slight indications of FCI's scan-lines in Fig. 8b. These are noisy pixels that follow lines that run from East to West. The effect is more pronounced over water surfaces. In both figures, the effect of unidentified cloud pixels on the TCWV is visible through decreased TCWV at cloud edges. In contrast, there are some thin dust layers visible in the 475 North-Western and Central-Eastern parts of the RGBs, which do not show through in either of the TCWV products.

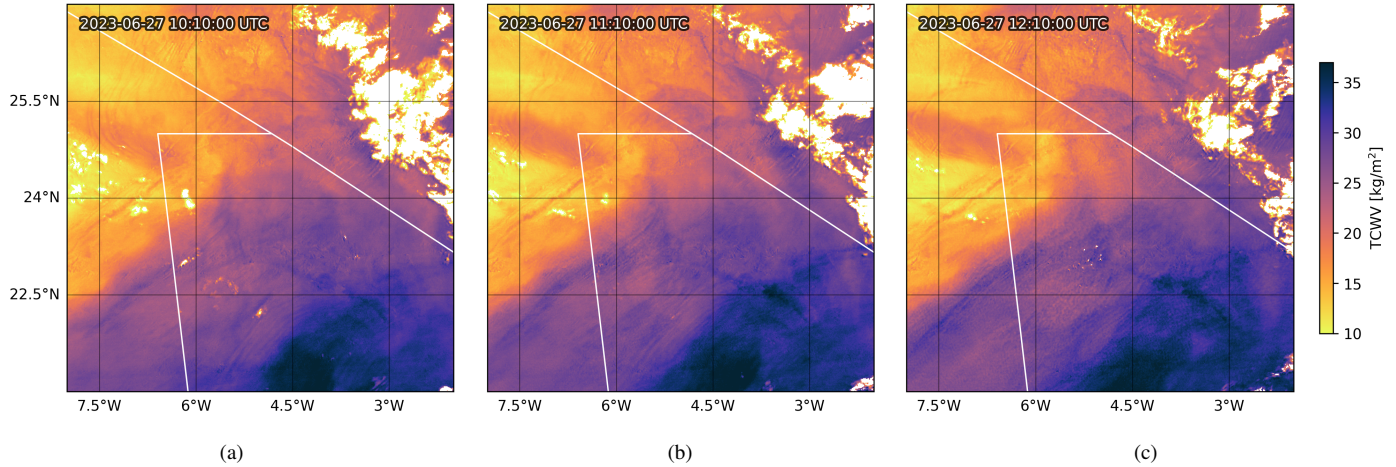


Figure 9. Time sequence of FCI TCWV shown in Fig. 8b with 1 hour between each frame.

To further highlight the potential of FCI TCWV observations for convective nowcasting purposes, we showcase the TCWV field from Fig. 8b again in 9 with the TCWV from two time steps later in Fig. 9a to 9c. The sequence demonstrates how one can track the propagation of the gravity waves and the north-western movement of the moist airmass along the moisture-front. The formation of what appear to be small updrafts or thermals is indicated by stark increases in TCWV from Fig. 9b to 9c. 480 This results in a pattern similar to convective rolls shown in Carbajal Henken et al. (2015). There, in the lower center, at around 11:40 UTC first clouds are forming.

5 Discussion and Outlook

In the multi-annual validation against the reference ARM SGP TCWV dataset (2016 – 2023), the OLCI 2-band TCWV shows a good performance with a bias of 1.848 kg/m^2 , RMSD of 2.235 kg/m^2 , cRMSD of 1.256 kg/m^2 , and high R^2 of 0.99. The 485 wet bias could be corrected following the procedure described in Preusker et al. (2021). In a comparison against their COWa algorithm applied to the same matchup dataset, they have a similar R^2 of 0.99 but a lower RMSD of 1.3 kg/m^2 , which may well be attributed to both the use of an additional absorption band at 940 nm and initial τ_{pTOA} -correction. Such a good performance against the reference TCWV is promising, however, for this comparison, τ_{pTOA} has been estimated from two window bands (i.e., the same way COWa estimates τ_{pTOA}).

490 For FCI, the accuracy of τ_{pTOA} and subsequently TCWV mostly hinges on the PCR's ability to estimate the spectral slope. As shown in Figs. 3a and 3b, the approximation shows a good performance against the next-best estimate, i.e., extrapolation

from two adjacent window bands using OLCI measurements, and exceeds the performance of just using the window band at 0.865 μm . Approximated nL_{TOA}^* may deviate from the reference nL_{TOA}^* on average by 1.5 % over land and 3.5 % over water. In rare cases the PCR failed. We assume that there may be several processes at play that require deeper investigations.

495 Miss-characterisations of the surface reflectance translate to an additional uncertainty of about 1 to 2 kg/m^2 . Nevertheless, these initial results demonstrate that our approach is effective and advancing well towards an operational TCWV retrieval framework for FCI.

The global comparison against the reference networks returned slightly lower performance indicators with R^2 between 0.98 to 0.99, bias between 0.33 to 2.84 kg/m^2 , MAPD between 6.64 and 18.36 %, RMSD between 1.49 to 3.6 kg/m^2 , and cRMSD between 1.46 to 2.21 kg/m^2 . The highest RMSD and bias are found in the comparison against AERONET, which is most likely due to AERONET's dry bias (Pérez-Ramírez et al., 2014). The OLCI/SLSTR matchup analysis shows a decreased performance against the multi-year matchup of only OLCI over ARM SGP. This is due to a reduced number of matchups over a shorter time span and a higher geographic spread. A more rigorous validation would require a longer time period. However, the aim of this assessment is to show that the PCR does not drastically reduce the algorithm's performance. The actual performance of FCI

500 TCWV may deviate from these verification results, since the spectral characteristics and calibration are different from OLCI. Future validation studies have to be conducted for further characterization, which may also lead to a more elaborate correction for initial τ_{pTOA} estimation.

To assess the functionality of the current algorithm prototype, we applied it to the mtgt505 FCI Level 1c test dataset provided by EUMETSAT. Conceptually, everything is in working order. The running times are close to or below the 5-minute mark

510 (FCI's nominal temporal resolution on a 2024 computer) and allow for a near-real-time and operational application of our TCWV algorithm. Full-disk comparisons show that the algorithm produces a sensible TCWV field. The relative difference between collocated ECMWF ERA5 reanalysis TCWV at 12 UTC and FCI TCWV product reveals a systematic dry bias of approximately 8%. We see three probable reasons for this systematic dry bias: 1) the bias might be related to the preliminary calibration of the FCI data, 2) the PCR systematically over-estimates the surface reflectance at 0.914 μm and thus τ is too low

515 and 3) undetected deficits in our LUTs. If this systematic bias persists and no underlying reason can be found, we may mitigate it using the empirical correction method described in Preusker et al. (2021). Furthermore, there are large-scale patterns of positive and negative deviations close to one another. Such patterns are to be expected in a comparison against model data and indicate that the model struggles with accurately capturing the advection of air masses in both space and time. The observed

520 TCWV fields might be closer to the actual state. FCI's TCWV AVK of almost 1 indicates a high sensitivity to the measurement and only a small contribution of prior knowledge. This is also referred to as the algorithm being independent from the NWP input. This is a key advantage of NIR-TCWV in contrast to other satellite-retrieved TCWV. The decreased TCWV AVK over water surfaces is caused by the much lower water surface reflectance in the NIR. In cases where the reflectance is close to 0, the retrieval is challenging. However, the OE may still provide an update of the a priori TCWV field. Over sunglint, the AVKs above 0.4 indicate that the retrieval is much more independent from the a priori and much more reliable.

525 Comparing OLCI and FCI TCWV up close, we can easily see that FCI TCWV matches the level of detail found in the OLCI TCWV product. For scenes over Europe, FCI's resolution will be slightly lower compared to OLCI's reduced resolution.

Yet, FCI's resolution will be significantly higher than SEVIRI's. The stripes of enhanced noise that run across the FCI TCWV image are caused by scan-lines of FCI. Similar scan-line artifacts are found in whisk-broom sensors, too, such as MODIS or VIIRS. Over land this is barely noticeable; however, over dark water pixels it is pronounced. This may change in future Level 530 1c processing versions.

The assessment exercises discussed above helped us identify several limitations and challenges regarding TCWV retrievals from FCI measurements. The presence of clouds is visible as pixels with considerably lower TCWV than their surrounding. A robust cloud mask is needed to filter out such pixels. At a later stage, such retrieved pixels may be used for an "above cloud" water vapour product. Such a product may then be used for the detection of WV entrainment into the stratosphere, e.g., in the 535 presence of overshooting tops (Setvák et al., 2008; Dauhut et al., 2018; Khordakova et al., 2022).

While over the vast majority of surface types, the PCR yields reliable nL_{TOA}^* , in some cases it deviates far from the reference. This may be addressed by extending the training dataset the PCs are calculated from.

Currently, we use a fixed aerosol type, height, and thickness. Under conditions violating these assumptions (e.g., a strong 540 dust outbreak), retrieval quality would be decreased. We consider to simulate for additional aerosol mixtures and aerosol layer heights. Furthermore, using AOT forecasts from the Copernicus Atmosphere Monitoring Service (CAMS) could improve the retrieval. Another issue is that over water surfaces, the inversion framework is under-determined: a measurement vector with only two elements ($nL_{TOA}(0.865 \mu\text{m})$, $\tau_{pTOA}(0.914 \mu\text{m})$) is opposed by a state vector with three elements (TCWV, AOT, WSP). Outside of sunglint, the influence of the wind speed is marginal, and AOT mainly increases the TOA signal (and thus 545 the forward model is not sensitive to changes of the windspeed), and inside sunglint the influence of a thin layer of aerosol is reduced. Because of that, the information content is relatively balanced, and the impact is slightly reduced. Nevertheless, over water surfaces, adding an additional third channel to the measurement vector (e.g., 0.51 or 1.61 μm) may also improve the performance.

With FCI, we are able to monitor the temporal evolution of these small-scale patterns at a resolution similar to OLCI's. This 550 allows for the tracking of large- and small-scale dynamics before, during, and after convective development. Such features and their changes (e.g., convergence zones, convective rolls, deepening boundary layers) contain potential information for nowcasting purposes. Furthermore, the patterns observed in FCI TCWV may also be tracked and used to retrieve lower level atmospheric motion vectors (AMV).

Our framework may be adapted to provide accurate TCWV retrievals for other sensors featuring at least two channels in 555 and around the $\rho\sigma\tau$ band. The National Oceanic and Atmospheric Administration (NOAA) is commissioning GeoXO Imager (GXI), the successor to the Advanced Baseline Imager (ABI) on the Geostationary Operational Environmental Satellite - 3rd generation (GOES), which will include a WV absorption band in the $\rho\sigma\tau$ region (Lindsey et al., 2024). Another future instrument soon to be launched into a polar orbit is METImage, flying onboard EUMETSAT's Meteorological Operational satellite second generation A (METOP-SG-A) (Phillips et al., 2016). METImage will enable NIR TCWV with a spatial resolution 560 of 500 m and global coverage every day. METImage will also provide O2A band measurements (around 0.76 μm), which can be used to reduce ambiguity due to shielding of cirrus or elevated aerosol layers. A NIR TCWV product from METImage may then be used in advanced synergies with sounders such as Infrared Atmospheric Sounder Interferometer - New Generation

(IASI-NG), which will also be flying on METOP-SG-A. IASI-NG is the successor of IASI, which provides all-sky temperature and humidity profiles with a slightly lower accuracy in the presence of clouds (Müller, 2017).

Furthermore, the Infrared Sounder (IRS) will be operating on MTG-S1, MTG-I1's sister satellite, and will cover the same field of view as FCI. This will enable a synergy between TCWV from FCI and the IRS humidity profile product. NIR TCWV could very well complement profile soundings for both IASI-NG and IRS: one shortcoming of these retrievals is their low or missing sensitivity to the lowest layers of the troposphere (below 1-2 km). Furthermore, their spatial resolution is in the order of tens of km, often insufficient for assessing small-scale weather patterns. A high-spatial resolution NIR TCWV product, sensitive to the whole column of air, could complement such sounding products perfectly, albeit in the absence of clouds. A synergy could consist of an updated layer product or a product that provides the moisture content of the lowest levels of the troposphere. Such synergy products could provide crucial insights into the meteorological conditions, such as the atmospheric instability, and improve the potential for the prediction of severe weather.

6 Conclusions

Leveraging our expertise in total column water vapour (TCWV) retrievals from Near-Infrared (NIR) measurements for various satellite-based passive imagers, we developed a new retrieval framework for the new Meteosat Third Generation Flexible Combined Imager (MTG-FCI) measurements. The use of OLCI/SLSTR synergy "FCI-like" data proved valuable for establishing and validating an adapted TCWV retrieval framework for MTG-FCI. It offers a realistic and reliable testbed that supports algorithm development ahead of the availability of a sufficiently long and calibrated FCI data record. Key challenges, such as the surface reflectance treatment in the WV absorption band, can be addressed in preparation for the large-scale application of the retrieval to FCI data.

The evaluation exercises highlight the robustness of the retrieval framework and helped identify specific challenges and limitations related to the MTG-FCI instrument, which can be further addressed with fully calibrated FCI data in the near future.

As the successor to MSG-SEVIRI, MTG-FCI boasts extended observational and spectral capabilities that promise significant advancements in weather and climate research and applications, particularly in the monitoring and study of atmospheric TCWV amounts and dynamics. Notably, FCI is the first geostationary satellite instrument with measurements in the NIR $\rho\sigma\tau$ WV absorption band. While SEVIRI TIR measurements allowed for the derivation of information on WV amounts mainly in higher parts of the troposphere, the FCI NIR WV absorption measurements exhibit the greatest sensitivity to WV amounts near the surface. This enables accurate and high temporal resolution observations of changes in moisture content in the lower troposphere. Consequently, these novel and comprehensive TCWV observations will enhance the (real-time) monitoring of atmospheric moisture distributions in the boundary layer, their evolution, and associated meteorological phenomena across regional to continental scales, with the potential to significantly advance nowcasting techniques.

Code availability. After further refinement, the code will be made available via the NWCSAF GEO software package via: <https://www.nwcsaf.org/nwc/geo-geostationary-near-real-time-v2021>

595 *Data availability.* OLCI/SLSTR data obtained from here: EUMETSAT. ERA5 data obtained from here: Copernicus Climate Change Service and Climate Data Store (2023). Satellite AOT obtained from Copernicus Climate Change Service and Climate Data Store (2019)

600 *Author contributions.* Conceptualization, J.E.K., C.C.H., R.P.; methodology, J.E.K., C.C.H., R.P.; software, R.P., J.E.K.; validation, J.E.K.; formal analysis, J.E.K., C.C.H., R.P.; investigation, J.E.K., C.C.H., R.P.; resources, J.E.K., C.C.H., R.P., X.C., J.F.; data curation, J.E.K.; writing—original draft preparation, J.E.K.; writing—review and editing, J.E.K., C.C.H., R.P., X.C., P.R.; visualization, J.E.K.; supervision, R.P.; project administration, X.C., P.R.; funding acquisition, J.E.K., C.C.H., R.P., P.R., J.F..

Competing interests. The authors declare no conflict of interest.

605 *Acknowledgements.* This research has been partially funded by the Satellite Application Facility in Support to Nowcasting and Very Short Range Forecasting (NWCSAF) of the European Organisation for the Exploitation of Meteorological Satellites (EUMETSAT) through the Associated Visiting Activity NWC_AV23_01, by EUMETSAT COWa Contract EUM/CO/18/4600002115/EJK, by EUMETSAT FRAME Contract EUM/CO/24/4600002869/JoSt and by the Deutsche Forschungsgemeinschaft (DFG, German Research Foundation) - Project number: 320397309 (TP2 QPN) within FOR 2589 "Near-Realtime Quantitative Precipitation Estimation and Prediction" (RealPEP). We acknowledge the legacy and software of COWa that went into this algorithm, supported by the Remote Sensing Products (RSP) division of EUMETSAT. We thank NWCSAF and EUMETSAT for the provision of preliminary MTG-FCI data. We thank all researchers and staff for establishing and maintaining the AERONET Sites, SUOMINET Sites and ARM Sites used in this investigation.

Variable	Definition/ Explanation
A	averaging kernel matrix
a	τ_{pTOA} correction offset
b	τ_{pTOA} correction slope
ALB	surface albedo, i.e., surface irradiance reflectance
AMF	air mass factor
AVK	averaging kernel
c_{win}	regression coefficient vector
ε	forward model uncertainty
ε_{intp}	nL_{TOA}^* approximation uncertainty
F	forward model
F_0	spectral solar irradiance
G	gain matrix
K	jacobian matrix
λ	wavelength
L_{TOA}	top-of-atmosphere radiance
nL_{TOA}	normalised top-of-atmosphere radiance
nL_{TOA}^*	normalised top-of-atmosphere radiance corrected for WV attenuation
nL_{TOA}^{*ext}	nL_{TOA}^* estimated from extrapolation of window bands
nL_{TOA}^{*PCR}	nL_{TOA}^* estimated from principle component regression
p	parameter vector
r	spectral slope
R_{target}	reflectance vector of target
R_{win}	reflectance vector of window channels (source)
ρ	irradiance ratio reflectance
ρ_{TOA}	irradiance ratio reflectance at top-of-atmosphere
\hat{S}	retrieval error covariance matrix
S_a	a priori state error covariance matrix
S_ε	measurement error covariances matrix
SATA	satellite azimuth angle
SATZ	satellite zenith angle
SNR	signal to noise ratio
SUNA	sun azimuth angle
SUNZ	sun zenith angle
τ_{pTOA}	pseudo optical thickness
U_{target}	principle components folded to target band spectral response functions
U_{win}	principle components folded to window band spectral response functions
RAZI	relative azimuth angle
RAZI	relative azimuth angle
x	state vector
\hat{x}	true state vector
x_a	a priori state vector
x	state vector
y	measurement vector

Table A1. List of variables and their respective explanations.

610 **References**

Ackerman, S., Frey, R., Strabala, K., Liu, Y., Liam, G., Baum, B., and Menzel, P.: Discriminating Clear-Sky from Cloud with MODIS—Algorithm Theoretical Basis Document (MOD35), ATBD Reference Number: ATBD-MOD-06, Goddard Space Flight Center, Tech. rep., NASA, accessed: 2024-08-29, 2002.

Albert, P., Bennartz, R., Preusker, R., Leinweber, R., and Fischer, J.: Remote Sensing of Atmospheric Water Vapor Using the Moderate Resolution Imaging Spectroradiometer, <http://www.cloudmap.>, 2005.

615 Allen, M. R. and Ingram, W. J.: Constraints on future changes in climate and the hydrologic cycle, *Nature*, 419, <https://doi.org/10.1038/nature01092>, 2002.

Anderson, G. P., Clough, S. A., Kneizys, F. X., Chetwynd, J. H., and Shettle, E. P.: AFGL atmospheric constituent profiles (0-120km), AFGL-TR-86-0110 (OPI), 1986.

620 Benevides, P., Catalao, J., and Miranda, P. M.: On the inclusion of GPS precipitable water vapour in the nowcasting of rainfall, *Natural Hazards and Earth System Sciences*, 15, 2605–2616, <https://doi.org/10.5194/nhess-15-2605-2015>, 2015.

Bennartz, R. and Fischer, J.: Retrieval of columnar water vapour over land from backscattered solar radiation using the medium resolution imaging spectrometer, *Remote Sensing of Environment*, 78, 274–283, [https://doi.org/10.1016/S0034-4257\(01\)00218-8](https://doi.org/10.1016/S0034-4257(01)00218-8), 2001.

625 Cadeddu, M. P., Liljegren, J. C., and Turner, D. D.: The atmospheric radiation measurement (ARM) program network of microwave radiometers: Instrumentation, data, and retrievals, *Atmospheric Measurement Techniques*, 6, 2359–2372, <https://doi.org/10.5194/amt-6-2359-2013>, 2013.

Carbajal Henken, C., Dirks, L., Steinke, S., Diedrich, H., August, T., and Crewell, S.: Assessment of sampling effects on various satellite-derived integrated water vapor datasets using GPS measurements in Germany as reference, *Remote Sensing*, 12, <https://doi.org/10.3390/rs12071170>, 2020.

630 Carbajal Henken, C. K., Diedrich, H., Preusker, R., and Fischer, J.: MERIS full-resolution total column water vapor: Observing horizontal convective rolls, *Geophysical Research Letters*, 42, 10 074–10 081, <https://doi.org/10.1002/2015GL066650>, 2015.

Casadio, S., Castelli, E., Papandrea, E., Dinelli, B. M., Pisacane, G., Burini, A., and Bojkov, B. R.: Total column water vapour from along track scanning radiometer series using thermal infrared dual view ocean cloud free measurements: The Advanced Infra-Red WAter Vapour Estimator (AIRWAVE) algorithm, *Remote Sensing of Environment*, 172, 1–14, <https://doi.org/10.1016/j.rse.2015.10.037>, 2016.

635 Chen, J. and Dai, A.: The atmosphere has become increasingly unstable during 1979–2020 over the Northern Hemisphere, *Geophysical Research Letters*, 50, e2023GL106 125, 2023.

Copernicus Climate Change Service and Climate Data Store: Aerosol properties gridded data from 1995 to present derived from satellite observation, DOI:10.24381/cds.239d815c, accessed: 2024-09-02, 2019.

Copernicus Climate Change Service and Climate Data Store: ERA5 hourly data on single levels from 1940 to present, DOI:10.24381/cds.a 640 dbb2d47, accessed: 2024-08-30, 2023.

Cox, C. and Munk, W.: Measurement of the Roughness of the Sea Surface from Photographs of the Sun's Glitter, *Journal of the Optical Society of America*, 44, 838, <https://doi.org/10.1364/josa.44.000838>, 1954.

Dauhut, T., Chaboureau, J. P., Haynes, P. H., and Lane, T. P.: The mechanisms leading to a stratospheric hydration by overshooting convection, *Journal of the Atmospheric Sciences*, 75, 4383–4398, <https://doi.org/10.1175/JAS-D-18-0176.1>, 2018.

645 Diedrich, H., Preusker, R., Lindstrot, R., and Fischer, J.: Retrieval of daytime total columnar water vapour from MODIS measurements over land surfaces, *Atmospheric Measurement Techniques*, 8, 823–836, <https://doi.org/10.5194/amt-8-823-2015>, 2015.

Diedrich, H., Wittchen, F., Preusker, R., and Fischer, J.: Representativeness of total column water vapour retrievals from instruments on polar orbiting satellites, *Atmospheric Chemistry and Physics*, 16, 8331–8339, <https://doi.org/10.5194/acp-16-8331-2016>, 2016.

Donlon, C., Berruti, B., Buongiorno, A., Ferreira, M.-H., Féménias, P., Frerick, J., Goryl, P., Klein, U., Laur, H., Mavrocordatos, C., et al.:
650 The global monitoring for environment and security (GMES) sentinel-3 mission, *Remote Sensing of Environment*, 120, 37–57, 2012.

Doppler, L., Carbajal-Henken, C., Pelon, J., Ravetta, F., and Fischer, J.: Extension of radiative transfer code MOMO, matrix-operator model to the thermal infrared–Clear air validation by comparison to RTTOV and application to CALIPSO-IIR, *Journal of Quantitative Spectroscopy and Radiative Transfer*, 144, 49–67, 2014.

Dostalek, J. F., Grasso, L. D., Noh, Y.-J., Wu, T.-C., Zeitler, J. W., Weinman, H. G., Cohen, A. E. , and Lindsey, D. T.: Using GOES ABI Split-
655 Window Radiances to Retrieve Daytime Low-Level Water Vapor for Convective Forecasting, *E-Journal of Severe Storms Meteorology*, 16, 1–19, <https://doi.org/10.55599/ejssm.v16i2.79>, 2021.

Doswell, C. A., Brooks, H. E., and Maddox, R. A.: Flash Flood Forecasting: An Ingredients-Based Methodology, *Weather and Forecasting*, 11, 560–581, [https://doi.org/10.1175/1520-0434\(1996\)011<0560:FFFAIB>2.0.CO;2](https://doi.org/10.1175/1520-0434(1996)011<0560:FFFAIB>2.0.CO;2), 1996.

Durand, Y., Hallibert, P., Wilson, M., Lekouara, M., Grabarnik, S., Aminou, D., Blythe, P., Napierala, B., Canaud, J.-L., Pigouche, O.,
660 Ouaknine, J., and Verez, B.: The flexible combined imager onboard MTG: from design to calibration, *Sensors, Systems, and Next-Generation Satellites XIX*, 9639, 963 903, <https://doi.org/10.1117/12.2196644>, 2015.

El Kassar, J., Carbajal Henken, C., Preusker, R., and Fischer, J.: Optimal Estimation MSG-SEVIRI Clear-Sky Total Column Water Vapour Retrieval Using the Split Window Difference, *Atmosphere*, 12, 1256, <https://doi.org/10.3390/atmos12101256>, 2021.

EUMETSAT: EUMETSAT Data Store, <https://data.eumetsat.int/>.

665 EUMETSAT: MTGTD-505 FCI 1C Example Products for Compatibility Testing - Package Description, pp. 1–8, https://sftp.eumetsat.int/public/folder/UsCVknVOOkSyCdgpMimJNQ/User-Materials/Test-Data/MTG/MTG_FCI_L1C_RC72-20240113_TD-505_Feb2024/MTGTD-505FCI1CEExampleProductsforCompatibilityTesting-PackageDescription.pdf, 2024a.

EUMETSAT: New MTG FCI test dataset (MTGTD-505), <https://user.eumetsat.int/news-events/news/new-mtg-fci-test-dataset-mtgtd-505-2024b>.

670 Fabry, F.: The spatial variability of moisture in the boundary layer and its effect on convection initiation: Project-long characterization, *Monthly Weather Review*, 134, 79–91, 2006.

Fell, F. and Fischer, J.: Numerical simulation of the light field in the atmosphere–ocean system using the matrix-operator method, *Journal of Quantitative Spectroscopy and Radiative Transfer*, 69, 351–388, [https://doi.org/10.1016/S0022-4073\(00\)00089-3](https://doi.org/10.1016/S0022-4073(00)00089-3), 2001.

Fischer, J.: High resolution spectroscopy for remote sensing of physical cloud properties and water vapour, 1988.

675 Gao, B.-C. and J., K. Y.: The MODIS Near-IR Water Vapor Algorithm Product ID : MOD05 - Total Precipitable Water, Algorithm Technical Background Document, pp. 1–25, %5CBiblioteca_Digital_SPR%5CGao1992_ATBD.pdf, 1992.

Gao, B. C., Montes, M. J., Davis, C. O., and Goetz, A. F.: Atmospheric correction algorithms for hyperspectral remote sensing data of land and ocean, *Remote Sensing of Environment*, 113, <https://doi.org/10.1016/j.rse.2007.12.015>, 2009.

García-Pereda, J., Rípodas, P., Lliso, L., Calbet, X., Martínez, M., Lahuerta, A., Bartolomé, V., Gléau, H., Kerdraon, G., Péré, S., France, M.,
680 Moisselin, J.-M., Autones, F., Claudon, M., Jann, A., Wirth, A., Alonso, O., Fernandez, L., and Gallardo, J.: Use of NWCSAF NWC/GEO software package with MSG, Himawari-8/9 and GOES-13/16 satellites, in: EUMETSAT/AMS/NOAA, October, Boston, USA, 2019.

Hersbach, H., Bell, B., Berrisford, P., Hirahara, S., Horányi, A., Muñoz-Sabater, J., Nicolas, J., Peubey, C., Radu, R., Schepers, D., Simmons, A., Soci, C., Abdalla, S., Abellán, X., Balsamo, G., Bechtold, P., Biavati, G., Bidlot, J., Bonavita, M., Chiara, G. D., Dahlgren, P., Dee, D., Diamantakis, M., Dragani, R., Flemming, J., Forbes, R., Fuentes, M., Geer, A., Haimberger, L., Healy, S., Hogan, R. J.,

685 Hólm, E., Janisková, M., Keeley, S., Laloyaux, P., Lopez, P., Lupu, C., Radnoti, G., de Rosnay, P., Rozum, I., Vamborg, F., Vil-
laume, S., and Thépaut, J. N.: The ERA5 global reanalysis, *Quarterly Journal of the Royal Meteorological Society*, 146, 1999–2049,
<https://doi.org/10.1002/qj.3803>, 2020.

Hess, M., Koepke, P., and Schult, I.: Optical Properties of Aerosols and Clouds: The Software Package OPAC, *Bulletin of the American
Meteorological Society*, 79, 831–844, [https://doi.org/10.1175/1520-0477\(1998\)079<0831:OPOAAC>2.0.CO;2](https://doi.org/10.1175/1520-0477(1998)079<0831:OPOAAC>2.0.CO;2), 1998.

690 Hogan, R. J. and Matriardi, M.: Evaluating and improving the treatment of gases in radiation schemes: The Correlated K-Distribution
Model Intercomparison Project (CKDMIP), *Geoscientific Model Development*, 13, 6501–6521, [https://doi.org/10.5194/gmd-13-6501-2020](https://doi.org/10.5194/gmd-13-6501-
2020), 2020.

Holben, B. N., Eck, T. F., Slutsker, I., Tanré, D., Buis, J. P., Setzer, A., Vermote, E., Reagan, J. A., Kaufman, Y. J., Nakajima, T., Lavenu,
F., Jankowiak, I., and Smirnov, A.: AERONET—A federated instrument network and data archive for aerosol characterization, *Remote
Sensing of Environment*, 66, 1–16, [https://doi.org/10.1016/S0034-4257\(98\)00031-5](https://doi.org/10.1016/S0034-4257(98)00031-5), 1998.

695 Hollstein, A. and Fischer, J.: Radiative transfer solutions for coupled atmosphere ocean systems using the matrix operator technique, *Journal
of Quantitative Spectroscopy and Radiative Transfer*, 113, 536–548, <https://doi.org/10.1016/j.jqsrt.2012.01.010>, 2012.

Holmlund, K., Grandell, J., Schmetz, J., Stuhlmann, R., Bojkov, B., Munro, R., Lekouara, M., Coppens, D., Viticchie, B., August, T., et al.:
700 Meteosat Third Generation (MTG): Continuation and innovation of observations from geostationary orbit, *Bulletin of the American
Meteorological Society*, 102, E990–E1015, 2021.

Hu, J., Tang, S., Liu, H., and Min, M.: An operational precipitable water vapor retrieval algorithm for Fengyun-2F/VLSSR using a modified
three-band physical split-window method, *Journal of Meteorological Research*, 33, 276–288, <https://doi.org/10.1007/s13351-019-8111-4>,
2019.

Hünerbein, A., Bley, S., Horn, S., Deneke, H., and Walther, A.: Cloud mask algorithm from the EarthCARE Multi-Spectral Imager: the
705 M-CM products, *Atmospheric Measurement Techniques*, 16, 2821–2836, <https://doi.org/10.5194/amt-16-2821-2023>, 2023.

Iannone, R. Q., Niro, F., Goryl, P., Dransfeld, S., Hoersch, B., Stelzer, K., Kirches, G., Paperin, M., Brockmann, C., Gomez-Chova, L.,
Mateo-Garcia, G., Preusker, R., Fischer, J., Amato, U., Serio, C., Gangofner, U., Berthelot, B., Iordache, M. D., Bertels, L., Wolters,
E., Dierckx, W., Benhadj, I., and Swinnen, E.: Proba-V cloud detection Round Robin: Validation results and recommendations, 2017
9th International Workshop on the Analysis of Multitemporal Remote Sensing Images, MultiTemp 2017, [https://doi.org/10.1109/Multi-Temp.2017.8035219](https://doi.org/10.1109/Multi-
710 Temp.2017.8035219), 2017.

Johns, R. H. and Doswell, C. A.: Severe Local Storms Forecasting, *Weather and Forecasting*, 7, 588–612, [https://doi.org/10.1175/1520-0434\(1992\)007<0588:SLSF>2.0.CO;2](https://doi.org/10.1175/1520-
0434(1992)007<0588:SLSF>2.0.CO;2), 1992.

Khordakova, D., Rolf, C., Grooß, J. U., Müller, R., Konopka, P., Wieser, A., Krämer, M., and Riese, M.: A case study on the impact of severe
convective storms on the water vapor mixing ratio in the lower mid-latitude stratosphere observed in 2019 over Europe, *Atmospheric
715 Chemistry and Physics*, 22, 1059–1079, <https://doi.org/10.5194/acp-22-1059-2022>, 2022.

Kleespies, T. J. and McMillin, L. M.: Retrieval of precipitable water from observations in the split window over varying sur-
face temperatures, *Journal of Applied Meteorology and Climatology*, 29, 851–862, [https://doi.org/10.1175/1520-0450\(1990\)029<0851:ROPWFO>2.0.CO;2](https://doi.org/10.1175/1520-
0450(1990)029<0851:ROPWFO>2.0.CO;2), 1990.

Knist, C., Kayser, M., Löffler, M., Vural, J., Schomburg, A., Görsdorf, U., Lauermann, F., Leinweber, R., Klink, S., and Lehmann, V.: DWD
720 Pilotstation - Evaluating ground-based remote sensing systems for future observing networks, <https://doi.org/10.5194/ems2022-119>, 2022.

Koenig, M. and De Coning, E.: The MSG global instability indices product and its use as a nowcasting tool, *Weather and Forecasting*, 24,
272–285, <https://doi.org/10.1175/2008WAF222141.1>, 2009.

Langley, S. P.: Annals of the Astrophysical Observatory of the Smithsonian Institution, Volume I., *Monthly Weather Review*, 30, 258–260, <https://doi.org/10.1175/1520-0493-30.5.258>, 1902.

725 Lindsey, D. T., Grasso, L., Dostalek, J. F., and Kerkmann, J.: Use of the GOES-R split-window difference to diagnose deepening low-level water vapor, *Journal of Applied Meteorology and Climatology*, 53, 2005–2016, <https://doi.org/10.1175/JAMC-D-14-0010.1>, 2014.

Lindsey, D. T., Bikos, D., and Grasso, L.: Using the GOES-16 split window difference to detect a boundary prior to cloud formation, *Bulletin of the American Meteorological Society*, 99, 1541–1544, <https://doi.org/10.1175/BAMS-D-17-0141.1>, 2018.

Lindsey, D. T., Heidinger, A. K., Sullivan, P. C., McCorkel, J., Schmit, T. J., Tomlinson, M., Vandermeulen, R., Frost, G. J., Kondragunta, S., and Rudlosky, S.: GeoXO NOAA's Future Geostationary Satellite System, *Bulletin of the American Meteorological Society*, 105, E660–E679, <https://doi.org/10.1175/BAMS-D-23-0048.1>, 2024.

Lindstrom, R., Preusker, R., Diedrich, H., Doppler, L., Bennartz, R., and Fischer, J.: 1D-Var retrieval of daytime total columnar water vapour from MERIS measurements, *Atmospheric Measurement Techniques*, 5, 631–646, <https://doi.org/10.5194/amt-5-631-2012>, 2012.

730 Lyapustin, A., Alexander, M. J., Ott, L., Molod, A., Holben, B., Susskind, J., and Wang, Y.: Observation of mountain lee waves with MODIS NIR column water vapor, *Geophysical Research Letters*, 41, 710–716, <https://doi.org/10.1002/2013GL058770>, 2014.

735 Martin, P. P., Durand, Y., Aminou, D., Gaudin-Delrieu, C., and Lamard, J.-L.: FCI instrument on-board MeteoSat Third Generation satellite: design and development status, in: *International Conference on Space Optics—ICSO 2020*, vol. 11852, pp. 125–140, SPIE, 2021.

Martinez, M. A., Calbet, X., and Ripodas, P.: Scientific and Validation Report for the iSHAI Processors of the NWC/GEO, https://www.nw-csaf.org/Downloads/GEO/2021/Documents/Scientific_Docs/NWC-CDOP3-GEO-AEMET-SCI-VR-iSHAI_v2.0.pdf, 2022.

740 Mather, J. H. and Voyles, J. W.: The arm climate research facility: A review of structure and capabilities, *Bulletin of the American Meteorological Society*, 94, 377–392, <https://doi.org/10.1175/BAMS-D-11-00218.1>, 2013.

Meerdink, S. K., Hook, S. J., Roberts, D. A., and Abbott, E. A.: The ECOSTRESS spectral library version 1.0, *Remote Sensing of Environment*, 230, 111 196, <https://doi.org/10.1016/j.rse.2019.05.015>, 2019.

745 Müller, J.: MSG Level 1.5 image data format description, EUM/MSG/ICD/105, p. 127, https://www-cdn.eumetsat.int/files/2020-05/pdf_te_n_05105_msg_img_data.pdf, 2017.

Neelin, J. D., Martinez-Villalobos, C., Stechmann, S. N., Ahmed, F., Chen, G., Norris, J. M., Kuo, Y. H., and Lenderink, G.: Precipitation Extremes and Water Vapor: Relationships in Current Climate and Implications for Climate Change, *Current Climate Change Reports*, 8, 17–33, <https://doi.org/10.1007/s40641-021-00177-z>, 2022.

750 Pérez-Ramírez, D., Whiteman, D. N., Smirnov, A., Lyamani, H., Holben, B. N., Pinker, R., Andrade, M., and Alados-Arboledas, L.: Evaluation of AERONET precipitable water vapor versus microwave radiometry, GPS, and radiosondes at ARM sites, *Journal of Geophysical Research*, 119, 9596–9613, <https://doi.org/10.1002/2014JD021730>, 2014.

Peters, J. M., Nielsen, E. R., Parker, M. D., Hitchcock, S. M., and Schumacher, R. S.: The impact of low-level moisture errors on model forecasts of an MCS observed during PECAN, *Monthly Weather Review*, 145, 3599–3624, 2017.

755 Phillips, P., Bonsignori, R., Schluessel, P., Schmülling, F., Spezzi, L., Watts, P., and Zerfowski, I.: Overview of calibration and validation activities for the EUMETSAT polar system: second generation (EPS-SG) visible/infrared imager (METImage), *Proc SPIE*, 10000, 100 000S–1, <https://doi.org/10.1117/12.2240938>, 2016.

Pinty, B. and Verstraete, M. M.: GEMI: a non-linear index to monitor global vegetation from satellites, *Vegetatio*, 101, 15–20, <https://doi.org/10.1007/BF00031911>, 1992.

Preusker, R., Henken, C. C., and Fischer, J.: Retrieval of daytime total column water vapour from OLCI measurements over land surfaces, 760 *Remote Sensing*, 13, 1–23, <https://doi.org/10.3390/rs13050932>, 2021.

Púčik, T., Groenemeijer, P., Rýva, D., and Kolář, M.: Proximity soundings of severe and nonsevere thunderstorms in central Europe, *Monthly Weather Review*, 143, 4805–4821, <https://doi.org/10.1175/MWR-D-15-0104.1>, 2015.

Rodgers, C. D.: Inverse methods for atmospheric sounding - theory and practice, 2, 238, <https://doi.org/10.1142/9789812813718>, 2000.

Rothman, L., Rinsland, C., Goldman, A., Massie, S., Edwards, D., Flaud, J.-M., Perrin, A., Camy-Peyret, C., Dana, V., Mandin, J.-Y.,
765 Schroeder, J., McCann, A., Gamache, R., Wattson, R., Yoshino, K., Chance, K., Jucks, K., Brown, L., Nemtchinov, V., and Varanasi, P.: The HITRAN Molecular Spectroscopic Database and HAWKS (HITRAN Atmospheric Workstation): 1996 Edition, *Journal of Quantitative Spectroscopy and Radiative Transfer*, 60, 665–710, [https://doi.org/10.1016/S0022-4073\(98\)00078-8](https://doi.org/10.1016/S0022-4073(98)00078-8), 1998.

Schmetz, J., Pili, P., Tjemkes, S., Just, D., Kerkmann, J., Rota, S., and Ratier, A.: An Introduction to Meteosat Second Generation (MSG), *Bulletin of the American Meteorological Society*, 83, 991–991, <https://doi.org/10.1175/bams-83-7-schmetz-1>, 2002.

770 Schmidt, G. A., Ruedy, R. A., Miller, R. L., and Lacis, A. A.: Attribution of the present-day total greenhouse effect, *Journal of Geophysical Research Atmospheres*, 115, 1–6, <https://doi.org/10.1029/2010JD014287>, 2010.

Setvák, M., Lindsey, D. T., Rabin, R. M., Wang, P. K., and Demeterová, A.: Indication of water vapor transport into the lower stratosphere above midlatitude convective storms: Meteosat Second Generation satellite observations and radiative transfer model simulations, *Atmospheric Research*, 89, 170–180, <https://doi.org/10.1016/j.atmosres.2007.11.031>, 2008.

775 Sisterson, D. L., Peppler, R. A., Cress, T. S., Lamb, P. J., and Turner, D. D.: The ARM Southern Great Plains (SGP) Site, *Meteorological Monographs*, 57, 6.1–6.14, <https://doi.org/10.1175/amsmonographs-d-16-0004.1>, 2016.

Skakun, S., Wevers, J., Brockmann, C., Doxani, G., Aleksandrov, M., Batič, M., Frantz, D., Gascon, F., Gómez-Chova, L., Hagolle, O., López-Puigdollers, D., Louis, J., Lubej, M., Mateo-García, G., Osman, J., Peressutti, D., Pflug, B., Puc, J., Richter, R., Roger, J. C., Scaramuzza, P., Vermote, E., Vesel, N., Zupanc, A., and Žust, L.: Cloud Mask Intercomparison eXercise (CMIX): An evaluation of cloud masking algorithms for Landsat 8 and Sentinel-2, *Remote Sensing of Environment*, 274, <https://doi.org/10.1016/j.rse.2022.112990>, 2022.

780 Thomas, G. E., Carboni, E., Sayer, A. M., Poulsen, C. A., Siddans, R., and Grainger, R. G.: Satellite Aerosol Remote Sensing over Land, January, <https://doi.org/10.1007/978-3-540-69397-0>, 2009.

Trenberth, K. E., Dai, A., Rasmusson, R. M., and Parsons, D. B.: The Changing Character of Precipitation, *Bulletin of the American Meteorological Society*, 84, 1205–1218, <https://doi.org/10.1175/BAMS-84-9-1205>, 2003.

785 Turner, D. D., Clough, S. A., Liljegren, J. C., Clothiaux, E. E., Cady-Pereira, K. E., and Gaustad, K. L.: Retrieving liquid water path and precipitable water vapor from the atmospheric radiation measurement (ARM) microwave radiometers, *IEEE Transactions on Geoscience and Remote Sensing*, 45, 3680–3689, <https://doi.org/10.1109/TGRS.2007.903703>, 2007.

Valdés, E. A. M., Morris, B. M., and Demory, B. O.: Monitoring precipitable water vapour in near real-time to correct near-infrared observations using satellite remote sensing, *Astronomy and Astrophysics*, 649, <https://doi.org/10.1051/0004-6361/202039629>, 2021.

790 Van Baelen, J., Reverdy, M., Tridon, F., Labbouz, L., Dick, G., Bender, M., and Hagen, M.: On the relationship between water vapour field evolution and the life cycle of precipitation systems, *Quarterly Journal of the Royal Meteorological Society*, 137, 204–223, <https://doi.org/10.1002/qj.785>, 2011.

Van Ulden, A. P. and Wieringa, J.: Atmospheric boundary layer research at Cabauw, *Boundary-Layer Meteorology*, 78, 39–69, <https://doi.org/10.1007/BF00122486>, 1996.

795 Vidot, J. and Borbás, É.: Land surface VIS/NIR BRDF atlas for RTTOV-11: Model and validation against SEVIRI land SAF albedo product, *Quarterly Journal of the Royal Meteorological Society*, 140, 2186–2196, <https://doi.org/10.1002/qj.2288>, 2014.

Ware, R. H., Fulker, D. W., Stein, S. A., Anderson, D. N., Avery, S. K., Clark, R. D., Droege, K. K., Kuettner, J. P., Minster, J. B., and Sorooshian, S.: Suominet: A real-time national GPS network for atmospheric research and education, *Bulletin of the American Meteorological Society*, 81, 677–694, [https://doi.org/10.1175/1520-0477\(2000\)081<0677:SARNGN>2.3.CO;2](https://doi.org/10.1175/1520-0477(2000)081<0677:SARNGN>2.3.CO;2), 2000.

800 Wevers, J., Müller, D., Scholze, J., Kirches, G., Quast, R., and Brockmann, C.: Sentinel-2 MSI IdePix ATBD, <https://zenodo.org/record/5788067>, 2021.

Wiegner, M. and Gasteiger, J.: Correction of water vapor absorption for aerosol remote sensing with ceilometers, *Atmospheric Measurement Techniques*, 8, 3971–3984, <https://doi.org/10.5194/amt-8-3971-2015>, 2015.